



Impact of Synoptic Wind Intensification and Relaxation on the Dynamics and Heat Budget of the South Senegalese Upwelling Sector

Pierre Chabert, Xavier Capet, Vincent Echevin, Alban Lazar, Christophe
Hourdin, Siny Ndoeye

► To cite this version:

Pierre Chabert, Xavier Capet, Vincent Echevin, Alban Lazar, Christophe Hourdin, et al.. Impact of Synoptic Wind Intensification and Relaxation on the Dynamics and Heat Budget of the South Senegalese Upwelling Sector. *Journal of Physical Oceanography*, 2023, 53 (4), pp.1041-1067. 10.1175/jpo-d-22-0092.1 . hal-04104114

HAL Id: hal-04104114

<https://hal.science/hal-04104114>

Submitted on 24 May 2023

HAL is a multi-disciplinary open access archive for the deposit and dissemination of scientific research documents, whether they are published or not. The documents may come from teaching and research institutions in France or abroad, or from public or private research centers.

L'archive ouverte pluridisciplinaire **HAL**, est destinée au dépôt et à la diffusion de documents scientifiques de niveau recherche, publiés ou non, émanant des établissements d'enseignement et de recherche français ou étrangers, des laboratoires publics ou privés.

Impact of Synoptic Wind Intensification and Relaxation on the Dynamics and Heat Budget of the South Senegalese Upwelling Sector

PIERRE CHABERT^a, XAVIER CAPET,^a VINCENT ECHEVIN,^a ALBAN LAZAR,^a CHRISTOPHE HOURDIN,^a
AND SINY NDOYE^b

^a *Sorbonne Université, CNRS, IRD, MNHN, Laboratoire d'Océanographie et du Climat: Expérimentations et Approches Numériques (LOCEAN-IPSL), Paris, France*

^b *Ecole Supérieure des Sciences et Techniques de l'Ingénieur (ESTI), Université Amadou Mahtar Mbow, Dakar, Senegal*

(Manuscript received 18 April 2022, in final form 24 November 2022)

ABSTRACT: In addition to their well-known seasonal cycle, eastern boundary upwelling systems (EBUS) undergo modulation on shorter synoptic to intraseasonal time scales. Energetic intensifications and relaxations of upwelling-favorable winds with 5–10-day typical time scales can impact the EBUS dynamics and biogeochemical functioning. In this work the dynamical effects of wind-forced synoptic fluctuations on the South Senegalese Upwelling Sector (SSUS) are characterized. The region geomorphology is unique with its wide continental shelf and a major coastline discontinuity at its northern edge. The ocean response to synoptic events is explored using a modeling framework that involves applying idealized synoptic wind intensification or relaxation to a five-member climatological SSUS ensemble run. Model evaluation against sparse midshelf in situ observations indicates qualitative agreement in terms of synoptic variability of temperature, stratification, and ocean currents, despite a moderate but systematic bias in current intensity. Modeled synoptic wind and heat flux fluctuations produce clear modulations of all dynamical variables with robust SSUS-scale and mesoscale spatial patterns. A mixed layer heat budget analysis is performed over the continental shelf to uncover the dominant processes involved in SSUS synoptic variability. Modulations of horizontal advection and atmospheric forcing are the leading-order drivers of heat changes during either wind intensification or relaxation while vertical dynamics is of primary importance only in a very localized area. Also, modest asymmetries in the oceanic responses to upwelling intensification and relaxation are only identified for meridional velocities. This brings partial support to the hypothesis that synoptic variability has a modest net effect on the climatological state and functioning of upwelling systems dynamics.


KEYWORDS: Eddies; Oceanic mixed layer; Synoptic-scale processes; Ocean models


1. Introduction

Eastern boundary upwelling system (EBUS) dynamics are driven by alongshore upwelling-favorable winds generating vertical transport of nutrients in the euphotic layer and primary production. Winds undergo a strong seasonal cycle in most EBUS (Chavez and Messié 2009), but they are also subjected to shorter intraseasonal (10–60 days) and synoptic fluctuations (5–10 days), typically in the form of wind intensity modulations (i.e., relaxations and intensifications), but also shifts in wind direction. Synoptic variability can have large effects on the variability of ocean physical and biogeochemical properties [e.g., off central Chile (Aguirre et al. 2014; Torres et al. 1999, 2002) and off the U.S. West Coast (Zhang et al. 2015; Shanks et al. 2014; Evans et al. 2015; Bane et al. 2007)]. As climate change may induce a reduction of synoptic

variability in the low-latitude portions of EBUS (Aguirre et al. 2019), it would also be useful to better understand its impact on the coastal ocean dynamics.

Since Send et al. (1987) (see also Send 1989) it is known that intensification and relaxations phases may not have symmetric effects on ocean properties. The effects of relaxations do not, in general, reverse those of intensifications. Thus, rectification by eddy-like terms (i.e., residual effects) are associated with synoptic fluctuations and the mean/climatological state and functioning of upwelling regions are distinct from what they would be in the absence of these fluctuations. Other forms of rectification effects include those due to mesoscale eddies on the general ocean or atmospheric circulation (Farneti et al. 2010), to ENSO in the Pacific Ocean (Okumura et al. 2017), to barotropic tides (Zimmerman 1986), and surface waves (i.e., the so-called Stokes drift, Curcic et al. 2016). Synoptic forcing rectification (or lack thereof) is tracer and location dependent (Kuebel Cervantes and Allen 2006; Largier et al. 2006). An important cause of asymmetry for upper-ocean heat content is the fact that vertical processes (advection and mixing) are large cooling terms during intense upwelling events, but get merely turned off during relaxation. For upper-ocean heat content in the Point Reyes–Bodega Bay upwelling sector (Send et al. 1987) the asymmetry also arises from the differential behavior of surface heat fluxes and alongshore heat advection. The latter is generally believed to be an important source of asymmetry wherever coastline and bathymetric irregularities (e.g., capes

 Denotes content that is immediately available upon publication as open access.

 Supplemental information related to this paper is available at the Journals Online website: <https://doi.org/10.1175/JPO-D-22-0092.s1>.

Corresponding author: Pierre Chabert, pierre.chabert@locean.ipsl.fr

DOI: 10.1175/JPO-D-22-0092.1

© 2023 American Meteorological Society. For information regarding reuse of this content and general copyright information, consult the [AMS Copyright Policy \(www.ametsoc.org/PUBSReuseLicenses\)](#).

and bays) produce complex time- and space-variable alongshore temperature gradients (Send et al. 1987) and quasi-standing flow features (Barth et al. 2005; Ramp et al. 2005; Narimousa and Maxworthy 1989).

Biogeochemical tracers (e.g., dissolved oxygen; Send and Nam 2012; Aguirre et al. 2021) and marine organisms (e.g., phyto- and zooplankton; Pitcher et al. 1991; García-Reyes et al. 2014) are also subjected to rectification. The biological response of the latter to synoptic fluctuations (Dorman et al. 2005; Wing et al. 1995; Morgan et al. 2018) may produce additional ecosystem asymmetries.

All this has important implications, including for interannual variability. For instance, it contributes to decoupling low-passed time-averaged upwelling indices and ecosystem functioning indicators such as enrichment in nutrients and primary/secondary production (García-Reyes et al. 2014). But other studies indicate a rather linear response of the ocean to upwelling wind intensifications and relaxations (Aguirre et al. 2014), hence little rectification associated with synoptic-scale wind variability. Coexistence of these contrasting results may be the consequence of distinct oceanographic and geomorphological contexts, but progress is needed on this topic. Having mesoscale turbulence time scales comparable to those of synoptic variability further complicates the problem (Marchesiello et al. 2003).

Despite the intensity of synoptic wind fluctuations in the Canary Current system (Desbiolles et al. 2014; Kounta Diop 2019), their effect on the ocean has received limited attention, except in the northern part of the system (Ramos et al. 2013; Ferreira Cordeiro et al. 2018; Relvas and Barton 2005; Lopes et al. 2014).

We strive to fill this gap for the southern Senegal upwelling sector situated at the southern end of the system and, thereby, increase the general knowledge on the subject. Other West African sectors would certainly deserve a similar attention (e.g., Cape Ghir, Western Sahara Bank, Cape Blanc, and Arguin Bank; see Fig. 1a).

In a nutshell, upwelling winds along West Africa are driven by the pressure gradient between the North Atlantic subtropical anticyclone, named the Azores high, and heat lows present on land. South of 15°–20°N, the position of the ITCZ is also determinant. Their seasonal evolutions are such that the SSUS upwelling season is mainly from November to June (Roy 1989) (with the July–October interruption being characterized by a monsoon regime). Atmospheric extratropical Rossby wave activity has been linked to wind synoptic variability but the mechanisms at play would need further clarification (Sultan and Janicot 2003; Kounta Diop 2019).

The SSUS northern limit is the sharp Cape Verde (hereinafter CV), which hosts the city of Dakar. Its southern limit is somewhat arbitrarily chosen at 12.5°N so that it also includes Gambian territorial waters. During the upwelling season, the major geomorphologic irregularity at CV (coastline and bathymetry, see Fig. 1) is responsible for a quasi-permanent sea surface temperature (SST) pattern composed of a cold upwelling tongue emanating from CV that is predominantly oriented north–south (Ndoye et al. 2014) and a warm inshore SST strip south of approximately 14.5°N (Roy 1998). Numerical simulations have revealed the extreme concentration of upwelling in

the northern part of the SSUS and the importance of along-shore/southward transport in the system (Ndoye et al. 2017). SSUS synoptic fluctuations have been documented using satellite observations (Ndoye et al. 2014) and in situ measurements (Capet et al. 2017). It is hypothesized in the latter study that alongshore advection is key to explain midshelf heat content synoptic fluctuations.

To make progress, we design a set of original numerical experiments in which synthetic synoptic forcing anomalies (intensifications and relaxations) are applied to the realistic regional model of Ndoye et al. (2017). We describe and analyze various aspects of the forced SSUS dynamical response, including sub-mesoscale activity and surface mixed layer (hereafter SML) heat content. Direct comparison between intensification and relaxation twin simulations (i.e., with similar initial state) offers a simple way to examine the natural leading-order source of synoptic rectification (but leaves aside effects due to complex wind histories, i.e., succession of intensifications and relaxations of variable duration). An ensemble run strategy is used to reduce uncertainties induced by intrinsic quasi-balanced activity. A particular focus is on intensification/relaxation asymmetries because they are indicative of rectification effects associated with synoptic variability.

The paper is organized as follows. Material and methods are presented in section 2. A brief model evaluation is proposed in section 3. The SSUS forced response to synoptic atmospheric fluctuations is presented in section 4. Mixed layer heat budget analyses are performed in section 5. Some sensitivity tests and model limitations are presented in section 6. We finish with a discussion and some concluding remarks in sections 7 and 8.

2. Methods

We develop a modeling framework that involves idealized synoptic wind intensification and relaxation. Their specific spatiotemporal patterns are chosen based on composite analyses presented below. The resulting forcing is applied to five-member climatological SSUS ensemble simulations carried out using CROCO.

a. Model settings and simulations

We use the Coastal and Regional Ocean Community model (CROCO, from <https://www.croco-ocean.org/>; Hilt et al. 2020), derived from Regional Ocean Modeling System (ROMS; Shchepetkin and McWilliams 2005, 2009). The model configuration presented in Ndoye et al. (2017) takes advantage of the AGRIF grid refinement capability (Debreu and Blayo 2008). A parent grid covers most of the Canary Current system with a spatial resolution of ~10 km. A child domain spans the Senegalese ocean with finer resolution ~2.5 km (Fig. 1a). The two grids are run alongside using two-way coupling (Debreu et al. 2012). For the sake of simplicity and coherency with future biogeochemical coupling, we do not use the diurnal shortwave cycle. The general model approach relies on two classes of simulations.

First, a 10-yr-long climatological simulation is run to obtain 1) an ensemble of physical initial states on which to apply

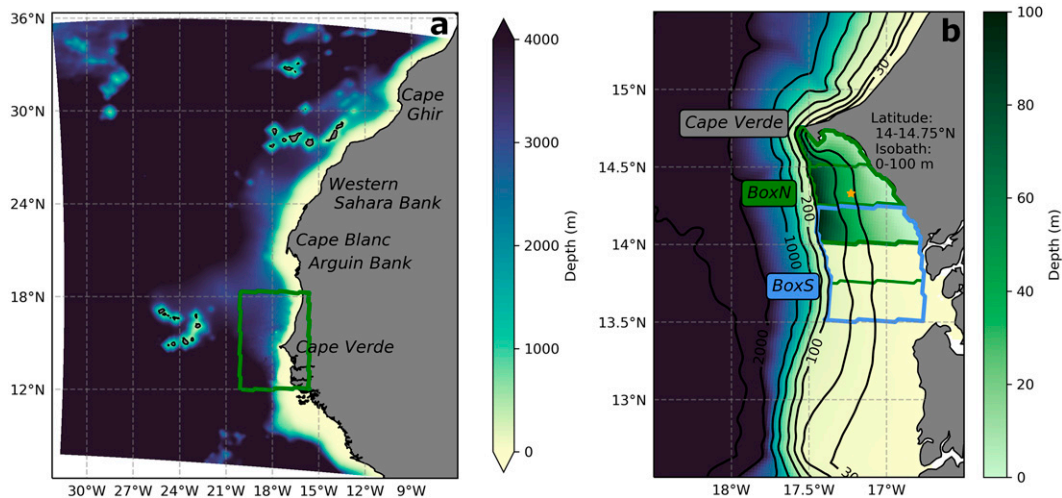


FIG. 1. (a),(b) Grid configuration used in the study. It consists of a parent domain encompassing most of the Canary Current system with a zoom at 2.5-km horizontal resolution over the Senegalese waters [green rectangle in (a); see text for details]. The study area located south of Cape Verde (SSUS) and various averaging boxes (green and blue solid lines) are shown in (b), as well as the Melax buoy location (orange star).

synoptic experiments and 2) model climatological average fields (noted with subscript climM) used for heat flux restoring to climatological SST (see [appendix A](#)). The climatological simulations are produced using monthly climatological surface heat fluxes from the International Comprehensive Ocean–Atmosphere Data Set (ICOADS; noted Q_{climO} ; years 1854–1992; spatial resolution $\Delta x = 0.5^\circ$; [Worley et al. 2005](#)), SST from the Moderate Resolution Imaging Spectroradiometer (MODIS; noted $\text{SST}_{\text{climO}}$; years 2002–18; $\Delta x = 5$ km; [NASA 2014](#)) for SST restoring, wind stress from the Scatterometer Climatology of Ocean Winds (SCOW; noted $\tau_{x|\text{climO}}$; $\tau_{y|\text{climO}}$; 1999–2009; $\Delta x = 0.25^\circ$; [Risien and Chelton 2008](#)), and open boundary conditions from the Simple Ocean Data Assimilation (SODA; over the period 2000–08; [Carton and Giese 2008](#)).

Second, a series of shorter synoptic runs (45 days) is performed for three different types of surface wind and air–sea heat flux anomalies: synoptic wind intensification, relaxation, and no anomaly (reference), denoted SF^+ , SF^- , and SF^0 , respectively. Subscript SF (resp. SF^\pm) refers to any synoptic forcing condition in $\{\text{SF}^+; \text{SF}^-; \text{SF}^0\}$ (resp., in $\{\text{SF}^+; \text{SF}^-\}$). The construction of forcing anomalies is described in the subsequent sections.

The standard vertical mixing scheme we use is the K -profile parameterization (KPP; [Large et al. 1994](#)), but we also explore the sensitivity of our results by carrying some runs with the k – ϵ ([Rodi 1987](#)) parameterization ([section 6a](#)).

b. ERA5 reanalysis dataset

Atmospheric synoptic conditions are expressed in terms of wind stress but also of net heat fluxes. As for other upwelling systems, the latter plays a noticeable role on the SSUS dynamics ([Ndoye et al. 2017](#); [Capet et al. 2017](#)). We use the ERA5 dataset from the European Centre for Medium-Range Weather Forecasts (ECMWF; [Hersbach et al. 2018](#); $\Delta x = 0.25^\circ$) to compute

synoptic wind stress and heat anomalies. We choose the temporal coverage between 2000 and 2010 to match the time period of the climatological wind stress we use (see [section 2a](#)) to force our model and obtain climatological physical states. We use the following variables: zonal and meridional wind speed at 10 m; shortwave and longwave radiation; and sensible and latent heat fluxes which are combined to provide net air–sea heat flux ([Barnier et al. 1995](#)). Wind stress is obtained from wind speed with the formula: $\tau = \rho_a C_D U_{10}^2$ with $\rho_a = 1.22 \text{ kg m}^{-3}$ the air density and $C_D = 0.0013$ the momentum transfer coefficient. For use in the compositing, a monthly climatology is built for wind stress and net heat flux, over the period 2000–10.

c. Idealized synoptic events

Zonal and meridional wind stress (τ_x ; τ_y) and net heat flux (Q) forcing fields are built as the sum of two separate terms (generically written for a field ϕ):

$$\phi_{\text{SF}^\pm}(x, y, t) = \phi_{\text{clim}}(x, y, t) + f(t) \times \phi'_{\text{SF}^\pm}(x, y). \quad (1)$$

Posing $\phi'_{\text{SF}^0} = 0$, Eq. (1) is also valid for SF^0 . The ϕ_{clim} is as described in [section 2a](#) for wind stress (see below and [appendix A](#) for heat flux). By construction, synoptic anomalies have a spatial structure that is fixed in time ϕ'_{SF^\pm} and a temporal modulation of their amplitude $f(t)$. The ϕ'_{SF^\pm} are defined based on ERA5 compositing.

1) COMPOSITES FIELDS $\phi'_{\text{SF}^\pm}(x, y)$

The composite analysis is restricted to the upwelling season defined as the period ranging from late October to late May. We consider that the ERA5 daily meridional wind stress (τ_y) is representative of the alongshore upwelling favorable winds over the SSUS ([Tall et al. 2021](#)). We average τ_y over the SSUS subdomain (19° – 16.5°W , 12.5° – 15.5°N) and remove the

seasonal cycle obtained with a low-pass Butterworth filter (with a threshold period of 115 days) to obtain the subseasonal wind stress anomaly $\delta\tau_y$.

Upwelling intensification (resp. relaxation) events are defined as the days during which $\delta\tau_y$ is below (resp. above) minus (resp. plus) one $\delta\tau_y$ standard deviation. We select $(\tau_x; \tau_y)$ and (Q) fields at these dates and remove the corresponding climatological monthly average (section 2b) to obtain an anomaly field. Finally, we construct a unique upwelling season anomaly ϕ'_{SF+} (resp. ϕ'_{SF-}) by averaging over all identified intensification (resp. relaxation) events (Figs. 2a–d).¹

The wind stress and heat flux anomalies present smooth regional scale patterns all over western Africa (Figs. 2c,d). Wind anomalies become weak south of 12°N so there will be little room for remotely generated SSUS upwelling/downwelling at synoptic scale (Philander and Yoon 1982).

The decomposition of the idealized events into shortwave and longwave radiation, sensible and latent heat flux are informative about atmospheric conditions during upwelling wind intensification or relaxation. The latent heat flux anomaly dominates the net heat flux anomaly: there is less (resp. more) evaporation, thus more heat loss (resp. more heat gain), during intensification (resp. relaxation) events (not shown), in agreement with previous studies describing atmospheric synoptic patterns (Garstang 1967; Desbiolles et al. 2014).

Because relaxation and intensification anomalies are quite similar and because it is convenient to use perfectly symmetric structures, we choose to ignore the composites obtained for relaxation events and define $\phi'_{SF-}(x, y) = -\phi'_{SF+}(x, y)$.

2) AMPLITUDE MODULATION $f(t)$

We now define the time modulation of amplitude $f(t)$. For simplicity we take $f(t)$ of the following form: two linear ramps, one upward and one downward with duration T_r each, and a plateau with constant wind stress anomaly between them with duration T_p . The choices made for T_r and T_p are key because they set the frequencies at which the SSUS dynamics will be perturbed. To provide general guidance a spectral analysis of the SSUS-averaged meridional wind stress (ERA5) was performed for nine upwelling seasons (defined between late October and late May of the following year). The mean spectrum does not reveal any synoptic time scale energetic peak but presents a distinctly shallower slope over the time range 10–12 days compared to longer time scales (not shown). In the following, we present simulations with $T_r = 3$ days, $T_p = 5$ days, and thus $T_{syn} = 2 \times T_r + T_p = 11$ days. Note that initial explorations for $T_{syn} = 6$ days produced dynamical and thermodynamical responses qualitatively similar to those with $T_{syn} = 11$ days but with smaller amplitude. As mentioned above, the wind stress direction is weakly affected by the synoptic fluctuation so little energy feeds near-inertial motions despite T_r being commensurate with the inertial frequency in the SSUS ($T_f = 2$ days). The idealized events are applied from 2 to 11 March included (hereinafter day 1 to

day 10) in the middle of the upwelling season (Roy 1989), a period of particular interest (Capet et al. 2017; Machu et al. 2019).

3) NET HEAT FLUX FORCING IMPLEMENTATION

The heat flux forcing in the synoptic runs can be written as

$$Q_{SF}(x, y, t) = Q_{clim}(x, y, t) + f(t) \times Q'_{SF}(x, y). \quad (2)$$

The construction of appropriate air–sea heat fluxes modulated during wind intensification and relaxation to force the synoptic simulations was made so as to respect three objectives/constraints: avoid artificial restoring to climatological SST during the synoptic runs; keep Q_{clim} close to the net air–sea heat flux diagnosed from our climatological run Q_{climM} and, in particular, prevent discontinuities at the restart time of the synoptic runs; have Q_{SF} independent of online model SST so that different members of an ensemble have the exact same Q forcing. The exact definition of $Q_{SF}(t)$ and more details are given in appendix A. The modulation of heat fluxes by synoptic events averaged over the SSUS is shown in Fig. 2. The evolution of Q_{clim} during that period of the year is also noticeable. The magnitude of $Q'_{SF}(t)$ is $\sim 40 \text{ W m}^{-2}$ at peak anomaly but a sensitivity to doubling Q'_{SF} is also presented (section 6). Choosing a symmetric form for Q'_{SF} is broadly consistent with the ERA5 composite analysis (which would yield a value 5 W m^{-2} smaller for the relaxation perturbation)² and facilitates the identification of asymmetries/synoptic rectification effects. Note that a minor preprocessing error led to an imperfect symmetry of the heat flux synoptic anomalies (Fig. 2). In BoxN (see Fig. 1b and section 2d), the typical effect of the erroneous heat flux (-5 W m^{-2} on average between days 1 and 15) on surface mixed layer temperature is estimated to be $\sim 0.07^\circ\text{C}$ and subsequently neglected.

d. Spatial averaging

Various forms of spatial averaging are used to identify responses to synoptic events. In particular, we define a northern (BoxN; see Fig. 1b) and a southern box (BoxS) in which we expect contrasted dynamics to occur. Their east–west delimitations are the coast and the 100-m isobath, respectively. We expect upwelling to mostly take place in BoxN delineated by the latitude 14.75°N (i.e., the Cape Verde Peninsula) and 14°N [see Fig. 2a in Ndoye et al. (2017), and our Fig. 8]. The southern box, in which lateral advection likely dominates, is delineated by latitudes 14.25° and 13.5°N. Alongshore averaging involves a simple remapping from longitude to water column depth with 5-m bins. It is performed over the gray area shown in Figs. 7 and 8, in the center of BoxN.

e. Ensemble experiment

1) ENSEMBLE APPROACH

Separating the oceanic response to synoptic atmospheric anomalies from intrinsic (primarily mesoscale) variability can be demanding in terms of available flow statistics (Marchesio et al. 2003;

¹ Northeasterly and northwesterly wind events were separated at an early stage of the study but produced similar ocean responses, so this distinction is ignored.

² In other upwelling regions surface heat fluxes may also be an important contributor to asymmetries (Send et al. 1987).

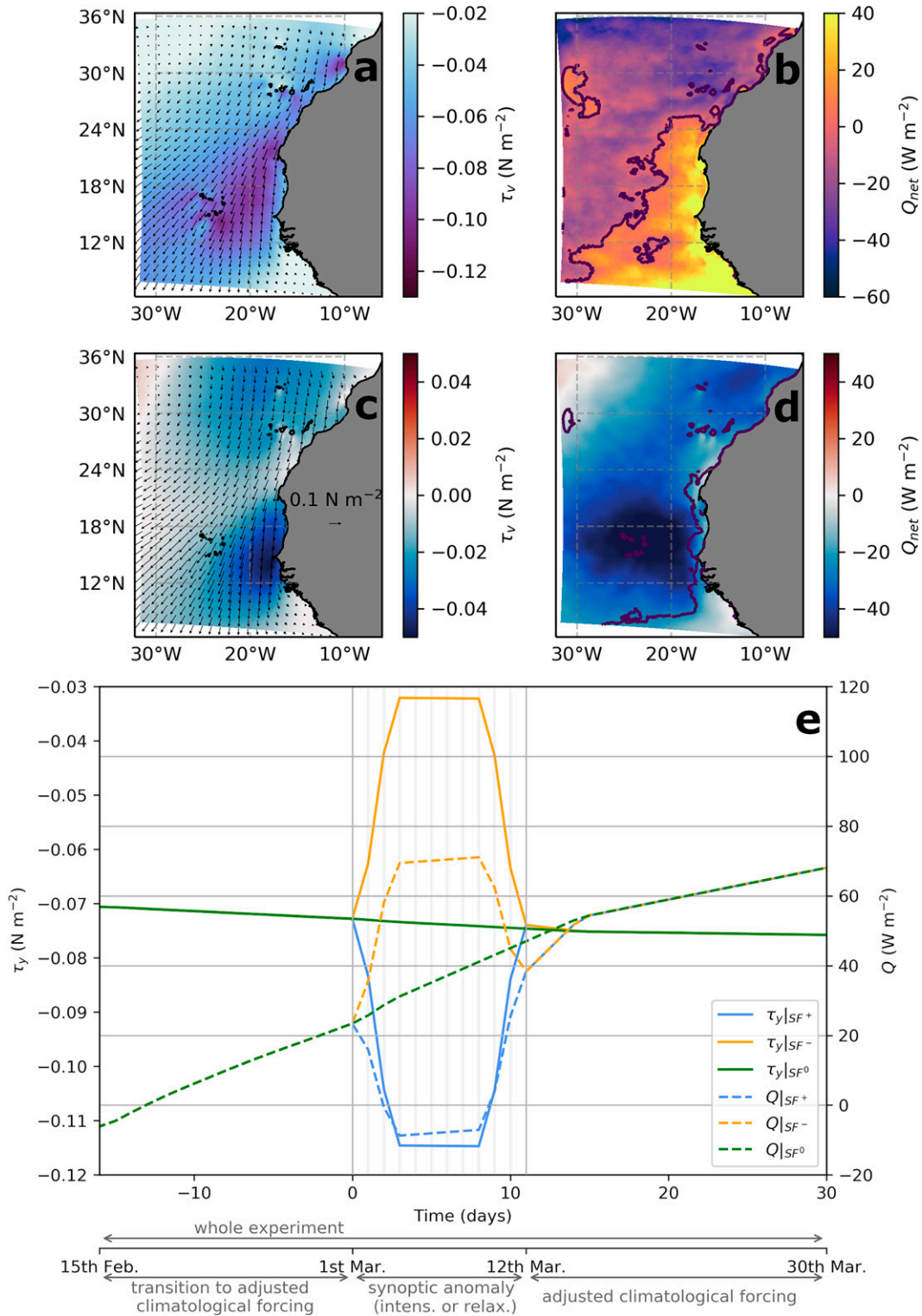


FIG. 2. Canary Current (a),(c) meridional wind stress and (b),(d) net heat fluxes climatological (SF^0) fields in (a) and (b) and SF^+ anomaly fields in (c) and (d) at the peak of the synoptic intensification. Anomalies for SF^- are the opposite of those for SF^+ . (e) The experimental timeline. Continuous (resp. dashed) lines indicate the evolution of the meridional wind stress (resp. net heat flux) averaged over the SSUS. Green (resp. blue and orange) lines are for climatological (resp. wind intensification and relaxation) forcings. A slight deviation from perfect $\text{SF}^+ - \text{SF}^-$ symmetry can be seen for heat fluxes, due to a small error. Its impact on simulated upper-ocean temperature is negligible (see section 2c).

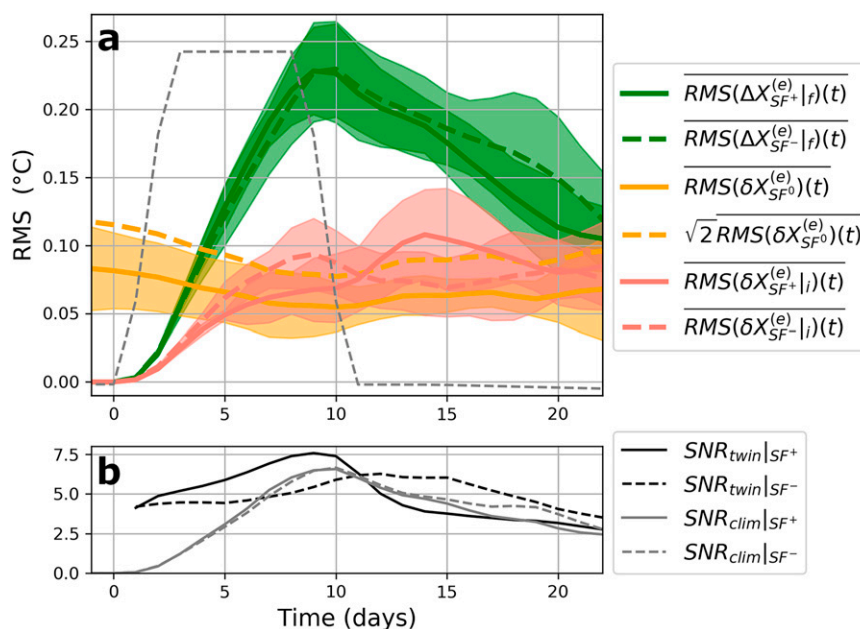


FIG. 3. (a) Time series of the ensemble averages of spatial RMS for various quantities computed for $X = \text{SST}$; see text in section 2e and Eq. (7). The gray dashed line represents the amplitude modulation of the synoptic anomaly $f(t)$. (b) Signal-to-noise ratios (SNR) as defined in section 2e.

Colas et al. 2013). We use an ensemble modeling approach to mitigate the effect of intrinsic variability and thus ascertain the SSUS deterministic response to synoptic wind events. Each ensemble run member (e) provides an independent system state scalar evolution $X^{(e)}(x, y, z, t)$.

The ensemble average is X_{SF} :

$$X_{\text{SF}} = \frac{1}{N_e} \sum_{e=1}^{N_e} X_{\text{SF}}^{(e)}(x, y, z, t) \quad (3)$$

with $(e) \in \{1; \dots; N_e\}$ the members on the ensemble. Mean synoptic anomalies are defined as the difference between synoptic and climatological ensemble averages ΔX_{SF^\pm} :

$$\Delta X_{\text{SF}^\pm} = X_{\text{SF}^\pm} - X_{\text{SF}^0}. \quad (4)$$

For each member, the deviation to the ensemble average $\delta X_{\text{SF}}^{(e)}$, i.e., the intrinsic variability part, is defined by

$$X_{\text{SF}}^{(e)} = X_{\text{SF}} + \delta X_{\text{SF}}^{(e)}. \quad (5)$$

By injecting Eq. (5) in Eq. (4), we obtain

$$\Delta X_{\text{SF}^\pm} = X_{\text{SF}^\pm}^{(e)} - \delta X_{\text{SF}^\pm}^{(e)} - (X_{\text{SF}^0}^{(e)} - \delta X_{\text{SF}^0}^{(e)}), \quad (6)$$

or also

$$\Delta X_{\text{SF}^\pm} = \underbrace{X_{\text{SF}^\pm}^{(e)} - X_{\text{SF}^0}^{(e)}}_{\Delta X_{\text{SF}^\pm}^{(e)} | f} - \underbrace{(\delta X_{\text{SF}^\pm}^{(e)} - \delta X_{\text{SF}^0}^{(e)})}_{\Delta X_{\text{SF}^\pm}^{(e)} | i}. \quad (7)$$

The mean forced response ΔX_{SF^\pm} due to synopticity can thus be written as the sum of a deterministic forced term $\Delta X_{\text{SF}^\pm}^{(e)} | f$ plus a term due to intrinsic variability $\delta X_{\text{SF}^\pm}^{(e)} | i$, and this equation is valid for each ensemble run. The intrinsic variability part would vanish when averaging over a sufficiently large ensemble, but we wish to choose a relatively small N_e for environmental/energy consumption reasons. The fact that we use identical initial conditions for the SF^\pm and reference climatological runs SF^0 is helpful in that regard because it limits the random scrambling due to turbulence compared to a situation where the initial states would be inconsistent between each other. In other words, we expect to have minimized the magnitude of $\delta X_{\text{SF}^\pm}^{(e)} | i$ relative to the magnitude of each term in its definition. To corroborate this, we show the RMS of the different terms in Eq. (7) for $X = \text{SST}$ in the shelf BoxN as a function of time (Fig. 3a). For each ensemble run, $\text{RMS}(\delta X_{\text{SF}^\pm}^{(e)} | i)$ grows from 0 at $t = 0$ days (when SF^+ and SF^0 simulations are identical) to $\approx \sqrt{2} \text{RMS}(\delta X_{\text{SF}^+}^{(e)}) \approx \sqrt{2} \text{RMS}(\delta X_{\text{SF}^0}^{(e)})$ at $t = 7$ days (this is also true when averaging over all ensemble members). Therefore, comparing synoptic and climatological twin simulations with identical initial conditions ameliorates the signal ($\Delta X_{\text{SF}^\pm}^{(e)} | f$) to noise ($\delta X_{\text{SF}^\pm}^{(e)} | i / \sqrt{N_e}$) ratio during the early part of the SF^\pm experiments, until day 11–12 for SF^+ and day 7 for SF^- as readily seen in Fig. 3b (see below section 4d on this SF^+/SF^- distinction). In practice choosing $N_e = 5$ appears appropriate to identify SSUS-scale evolutions (see Fig. 3b). More localized responses will be considered insofar as they emerge from noise with this relatively small ensemble, which guarantees that they are part of the first-order ocean response.

2) ROBUSTNESS OF THE DIAGNOSED FORCED OCEAN RESPONSE

At any given location, the anomalous response to synoptic forcings revealed by ensemble averaging will be considered robust if the following criterion is met:

$$\left| \sum_{e=1}^{N_e} \text{sign}(X_{\text{SF}^\pm}^{(e)} - X_{\text{SF}^0}^{(e)}) \right| = 5, \quad (8)$$

that is, if the synoptic anomaly is of the same sign in all ensemble members. When time and ensemble averaging are combined (e.g., to produce Figs. 6 and 7), the criterion must hold for each individual day of the time averaging window, which makes the criterion as stringent as possible.

f. Residual effect

In our idealized setting, we will infer the residual effect produced by synoptic variability as $\text{RES}_{\text{SF}}(X) = (1/2)(X_{\text{SF}^+} + X_{\text{SF}^-}) - X_{\text{SF}^0}$ for any oceanic variable X . We are also interested in the quantity $\mathcal{R}_{\text{SF}}(X) = \text{RES}_{\text{SF}}(X)/X_{\text{SF}^0} = [(1/2)(X_{\text{SF}^+} + X_{\text{SF}^-})/X_{\text{SF}^0}] - 1$, which quantifies the relative importance of the asymmetry. The term \mathcal{R}_{SF} will systematically be computed after ensemble and time averaging between day 3 and 8, i.e., during the plateau of SF^\pm forcing anomaly.

g. Heat budget

The clearest manifestation of synoptic variability is SST modulation. Based on vertical velocity fields shown in Ndoye et al. (2017) (see also our Fig. 8) and the minimum SST zone, we suspect that the role of vertical advection may be weak outside the northern sector of the SSUS. We perform an on-line heat budget to confirm this and more generally clarify the importance of the different processes at play in the temperature changes in the SML (as in Cambon 2008; Jullien et al. 2012; Echevin et al. 2018). The SML heat budget equation is

$$\underbrace{\langle \partial_t T \rangle}_{\text{RATE}} = \underbrace{-\langle \partial_x u T \rangle - \langle \partial_y v T \rangle}_{\text{HADV}} - \underbrace{\langle \partial_z w T \rangle}_{\text{VADV}} + \underbrace{\langle D_t(T) \rangle}_{\text{HMX}} + \underbrace{\langle D_z(T) \rangle}_{\text{VMIX+ENTR}} + \underbrace{\langle F(z) \rangle}_{\text{FORC}} \quad (9)$$

where T is the model potential temperature, the left term is the heating rate, (u, v, w) are the three-dimensional currents components. The right-hand side terms correspond to the advection in flux form (the total advection is noted $\text{ADV} = \text{HADV} + \text{VADV}$), horizontal and vertical mixing, entrainment/detrainment and heating/cooling due to surface heat fluxes. The term $\langle X \rangle = (1/h) \int_{-h}^0 X dz$ is the vertical averaging of the state scalar X over the time-dependent mixed layer depth (h) range.

A particular focus will be on advection because it is presumably important in driving the heat changes in the SSUS. Unfortunately, the interpretation of individual advection terms can be made difficult by the strong compensations between them (Gan and Allen 2005b; Colas et al. 2013). Incidentally, the

nondivergence of the flow, (i.e., $\partial_x u + \partial_y v + \partial_z w = 0$) implies that advection terms can be rewritten as follows:

$$-(\partial_x u T + \partial_y v T + \partial_z w T) = -[\partial_x u(T - T_0) + \partial_y v(T - T_0) + \partial_z w(T - T_0)], \quad (10)$$

with T_0 any arbitrary function of time only. A judicious choice for T_0 when studying the heat budget over a control volume \mathcal{V} is (Lentz 1987; Montgomery 1974):

$$T_0(t) = \frac{1}{V} \iiint_{\mathcal{V}} T(x, y, z, t) dV. \quad (11)$$

This is because, when volume averaging, every RHS term of Eq. (10) can be rewritten as a flux of tracer $(T - T_0)$ across \mathcal{V} interfaces, hence advection terms only contribute to the heat budget if/where they transport temperature anomalies. Compensations between the three terms are thus strongly reduced (see in the online supplemental material section 1). Advection terms of the volume average budgets described in section 5b are computed following this procedure.

h. Melax buoy data

To evaluate the model ability to reproduce shelf dynamics at seasonal and subseasonal time scales, we use in situ measurements from Melax mooring located over the shelf in ~ 35 -m water depth at $14^\circ 20.8' \text{N}$, $17^\circ 13.68' \text{W}$. An array of thermistors measured temperature at 11 depths every 30 s. An upward looking ADCP measured bottom temperature and horizontal current vertical profiles every 90 min with a vertical resolution of 1 m. The time series analyzed in this work extends from 11 February 2015 to 26 April 2016. For the sake of simplicity and given our interest in time scales of at least a few days, we degrade the temporal resolution of the data to 1 day. More details on data processing/availability and mooring characteristics are provided in appendix B and in Tall et al. (2021), respectively.

3. Model evaluation with in situ buoy measurements

a. Depth averaged currents

The model climatological and synoptic simulations are evaluated against in situ measurements at Melax. Following McCabe et al. (2015), we start by the simple comparison between modeled and observed daily depth averaged horizontal currents in March. The direction and intensity of the model currents is qualitatively consistent with observations (Fig. 4). Moderate biases are nevertheless noticeable, most conspicuously the lack of flow variability when climatological forcings are used. Including synoptic forcings leads to a much improved data-model agreement, as expected. Another bias is the overly intense southward flow in the model. Despite the fact that synoptic events do not change the averaged forcing, their incorporation also reduces (but does not entirely remove) this mean flow bias, for reasons that we clarify in section 4d. Importantly, note that wind relaxation appears necessary to produce barotropic poleward flows in CROCO (cf. Figs. 4a,b) but not in the ocean at Melax. This discrepancy may arise from the fact that

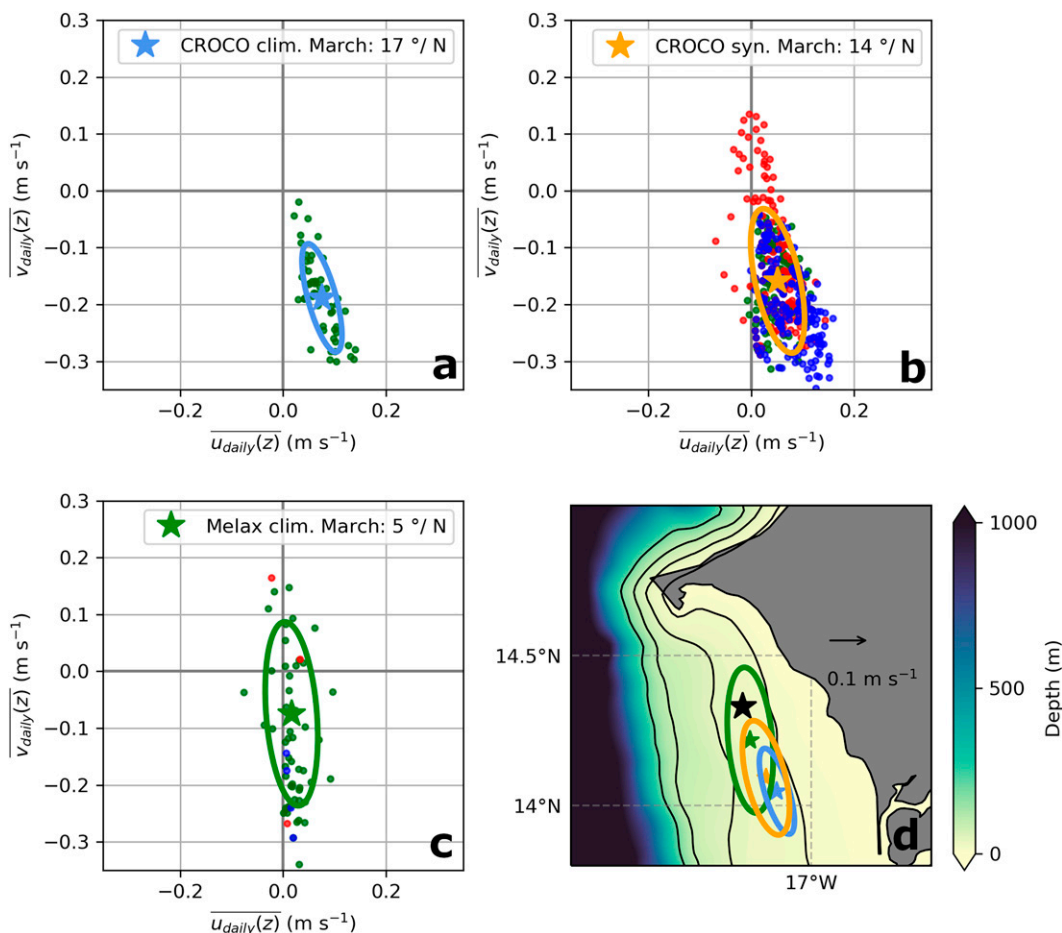


FIG. 4. The (u, v) depth averaged currents in (a) CROCO climatological simulations, (b) CROCO synoptic simulations, and (c) Melax (2015/16 observations). Each dot corresponds to one daily mean [5 days mean in (a)] current value for the month of March. The center of each ellipse materialized with a star indicates the mean current averaged over each available day while its semiaxes indicate the maximum and minimum variance. The angle between the ellipse major axis and north is indicated on top of each panel. In (b) and (c), blue (resp. red) dots correspond to daily currents at wind intensification (resp. relaxation) times. (d) Ellipses are all repeated for comparison, with the location of Melax (black star) as the origin ($u = v = 0$).

relaxation and upwelling conditions are less easily separated than in our idealized setting; our simulations ignore oceanic variability remotely generated outside our model grid. This being said, model and in situ data exhibit considerable variability in alongshore velocity for relaxation and intensification conditions (e.g., velocities ≈ -0.3 m s⁻¹ during relaxations).

b. Temperature vertical structure during synoptic events

The compositing method applied to ERA5 (see section 2b) is applied to Melax data. Wind measurements are used to identify synoptic relaxations and intensifications. Because we run idealized simulations, the model lacks variability and cannot reproduce the complexity of the real ocean. None exactly resembles our idealized events and most differ in important ways. Thus, we limit ourselves to a qualitative assessment of the model resemblance to observations during one intensification and one relaxation having wind anomaly extrema consistent with those of our

synthetic forcings (Fig. 5). Noticeable model–data differences are found in terms of overall wind forcing history (preintensification winds below average for the selected intensification event; absence of return to average wind conditions for the selected relaxation event) and initial ocean stratification. However, we note qualitative model–data agreement on synoptic thermal evolution including SML depth, and even on the magnitude of the temperature response to the first part of the relaxation event. Note that SML mean depth and its seasonal variability in our climatological simulations (~ 18 m; February–May) is roughly consistent with Melax observations [~ 14 m; note that including chlorophyll shading (Echevin et al. 2021) reduces the model SML depth to 16 m; not shown].

4. Synoptic SSUS dynamics

The circulation and thermohaline structure of the SSUS in response to synoptic forcing is not completely reorganized but

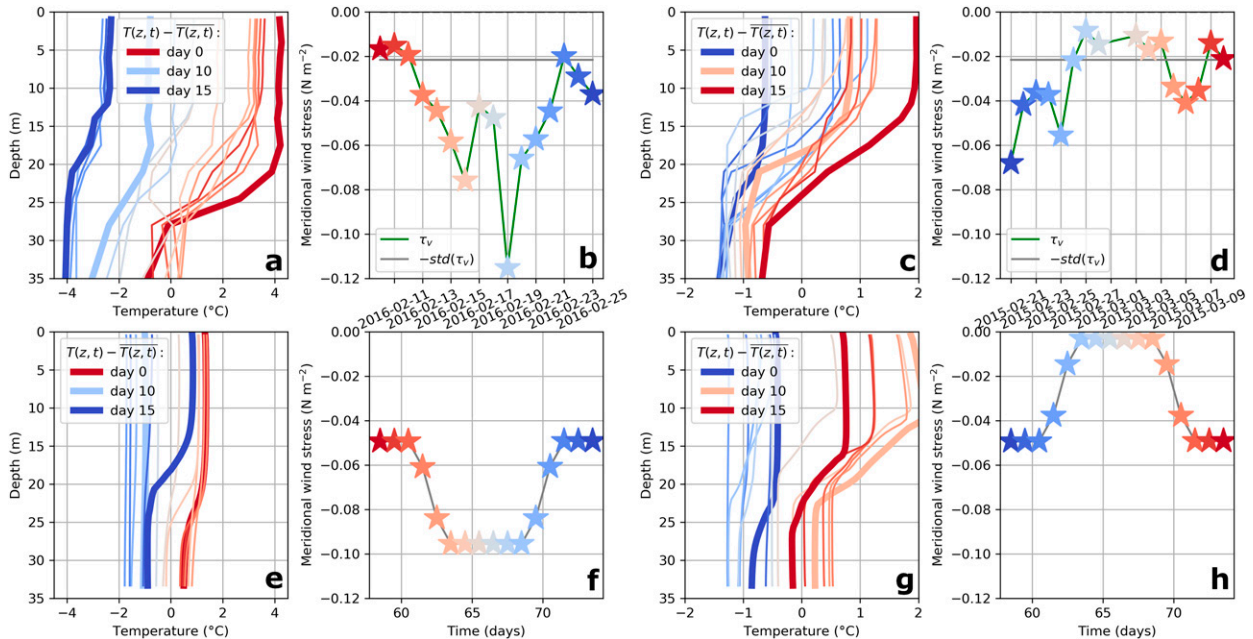


FIG. 5. (a),(c),(e),(g) Temperature anomaly profiles and (b),(d),(f),(h) wind evolution during intensification in (a), (b), (e), and (f) and relaxation events in (c), (d), (g), and (h). (top) Melax observations during two carefully chosen events and (bottom) ensemble averaged model solutions at Melax. The color codings of temperature profiles and of the wind time series are identical, which provides a time information to the former.

important modulations are found in terms of horizontal patterns and vertical structure. A careful evaluation of temporal evolutions also reveals asymmetrical responses between SF^+ and SF^- . The impact on the submesoscale variability is assessed.

a. Surface patterns of change

Patterns of change are generally consistent with expectations from theory. Over the southern Senegalese shelf, stronger (resp. weaker) winds lead to decreasing (resp. increasing) SSH and SST, and increasing southward (resp. decreasing southward or even reversing) flow (Figs. 6 and 7). SSH and SST patterns of change are very robust except SSTs during relaxation over the deeper part of the shelf. Over most of the shelf the SSH field has returned to near-climatological conditions for the period corresponding to days 19–22. This is less true for SST which exhibits anomalies whose magnitude remains comparable to that found during days 6–9, in particular for the relaxation experiments.

Examination of Figs. 6 and 7 (see also Figs. S2 and S3) also reveals the presence of mesoscale circulation features. In all simulations, an anticyclonic circulation tends to dominate the area just southwest of Cape Verde. This circulation is being reinforced during the active period of SF^+ (days 6–9) but this is a transient feature that is no longer visible at later times, hence is not associated with a coherent structure. On the other hand, SF^+ and SF^- each lead to the development of a relatively robust cyclonic eddy-like structure. For SF^+ , the cyclonic feature becomes visible at days 14–15. It remains centered around $13.5^\circ N$ while progressively drifting offshore.

This cyclone carries upwelled shelf waters and brings them offshore (see Fig. 7b). For SF^- , the cyclonic structure is already visible at days 6–9. Its center is located at $14.25^\circ N$, $17.6^\circ W$, near where the abovementioned anticyclonic circulation is generally located. This cyclone is associated with an offshore flow between Cape Verde and $14.5^\circ N$. It subsequently drifts northward and hugs the Cape Verde Peninsula around day 10, i.e., when normal upwelling winds resume. It is then absorbed/incorporated in the ensuing negative SSH anomalies and is transported offshore.

Examination of each individual SF^+ and SF^- run confirms this tendency to form cyclones made of recently upwelled shelf water and shed them offshore when winds relax, i.e., in the early part of SF^- and in the late part of SF^+ but with noticeable variations between ensemble runs. Shape, intensity, and exact offshore and alongshore location of these cyclonic features vary depending on the eddy field configuration over the continental slope and their evolution during the synoptic experiment. When large mesoscale features are present off the SSUS the formation of cyclones can even be inhibited. Cyclones produced in SF^- tend to be smaller, less robust, and more frequently absent in the different runs (cf. robustness information in Figs. 6b,f). We relate this to the fact that there must be more available potential energy (i.e., cold upper-ocean water) in SF^+ shortly after the upwelling wind intensification than there is in SF^- at the beginning of the relaxation. This description of the mesoscale field is helpful to understand some of the fine-scale features present in the SST field (see Figs. S2 and S3).

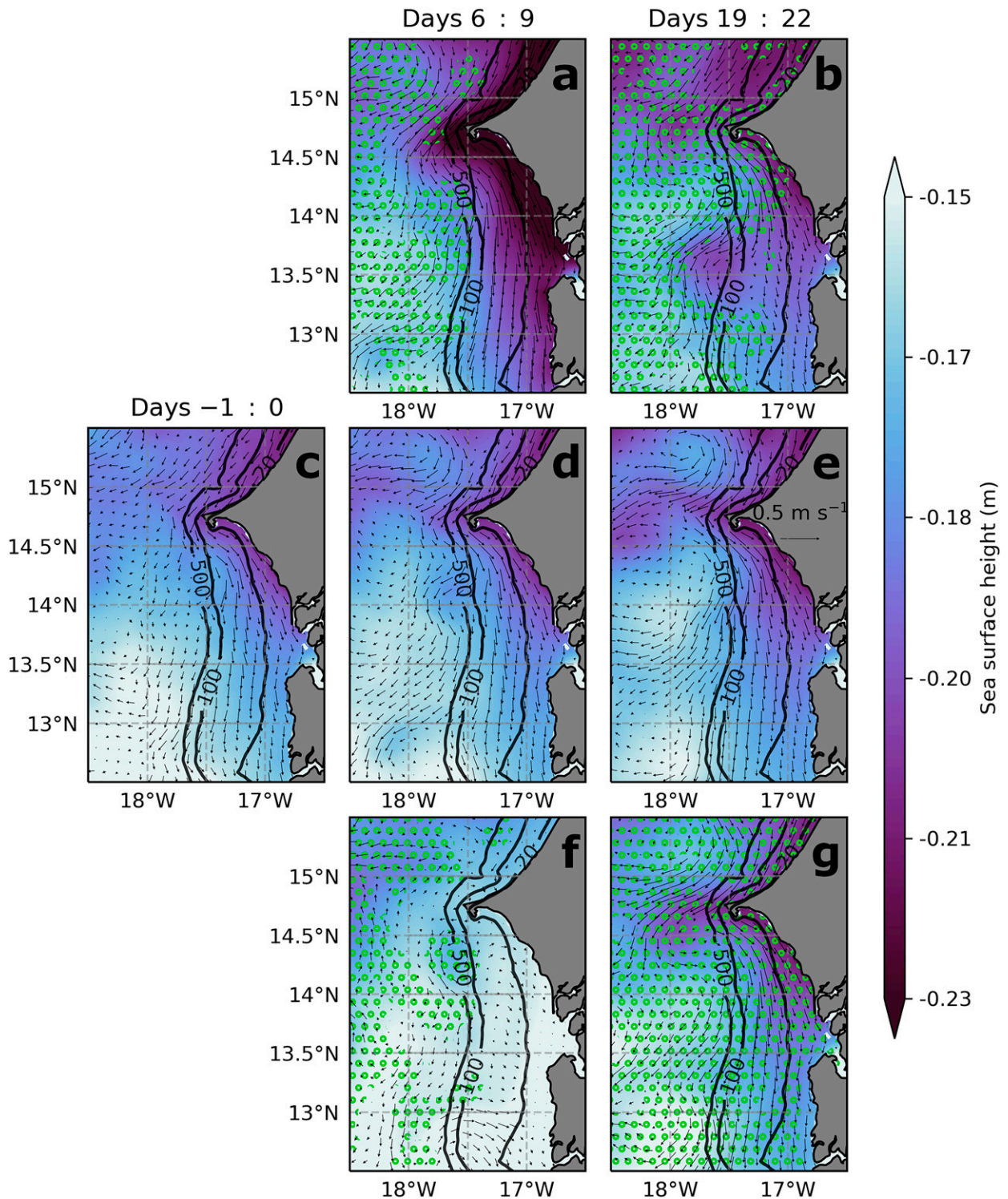


FIG. 6. Ensemble averaged fields of SSH (color) and surface velocity (arrows) for (a),(b) SF^+ , (c)–(e) SF^0 , and (f),(g) SF^- . The three periods (left) before (average of day -1 to day 0; see timeline and date reference in Fig. 2e), (center) during (days 6–9 included), and (right) after (days 19–22 included) the synoptic event. For the SF^+ and SF^- panels, light green circles indicate locations where not all ensemble members agree on the sign of the SSH anomaly relative to SF^0 (see section 2e).

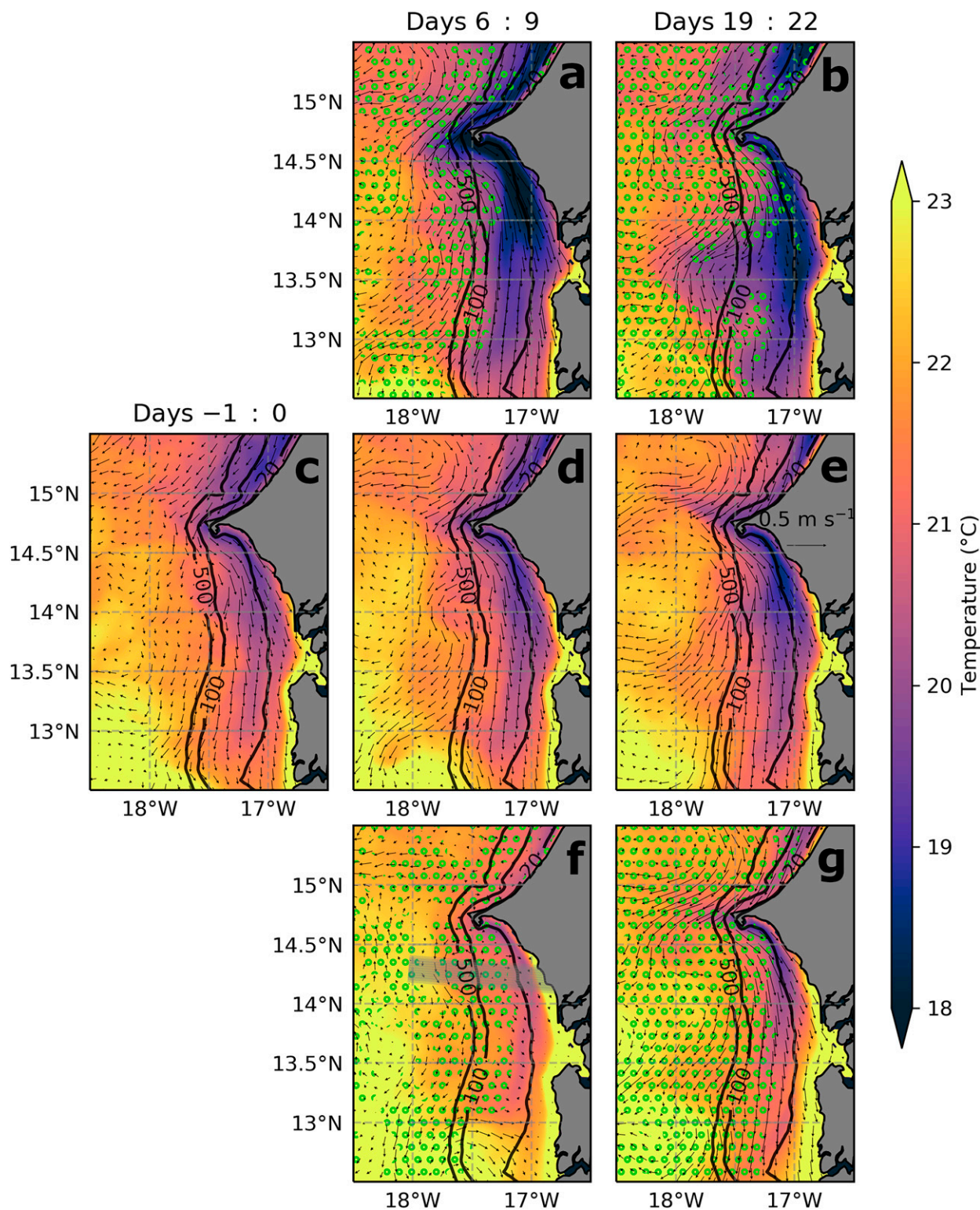


FIG. 7. As in Fig. 6, but for SST. The gray shading in (f) represents the sector over which along-isobath averaging is performed to obtain Fig. 9.

Vertical velocities at the base of the SML is an instructive field indicative of where upwelling takes place. Fields shown in Fig. 8 are quite noisy because averaging is performed over periods of a few days only. Nevertheless, the region within 25–50 km of Cape Verde systematically emerges as the place where largest vertical velocities occur (in agreement with Ndoye et al. 2017), and also where the modulation of their intensity by SF^+ and SF^- is most noticeable.

b. Vertical structure

The vertical structure of the dynamical response is described using cross-shore transects of temperature and meridional velocity (ensemble and alongshore averages, Fig. 9). We start with a brief characterization of the climatological state: SML depth ~ 30 m thick; offshore and coastal SST $\sim 21^\circ$ and 19.5°C , respectively (Fig. 9c); shoaling of isopycnals from offshore to nearshore of the order of 30 m; extension of the offshore equatorward upwelling jet (defined by the 0.1 m s^{-1} isotach) from the coast to ~ 60 km offshore (near 17.5°W); presence of a subsurface poleward current located offshore of 17.4°W and below ~ 40 -m depth; positive vertical velocities ($v \sim 2\text{ m day}^{-1}$) below the SML. All this illustrates the relative weakness of the southern Senegal upwelling in comparison to other well-known sectors where isopycnal tilts, across-shore temperature/density contrasts, and vertical velocities can be much greater [e.g., Renault et al. (2021) in the California upwelling system]. Our average synoptic intensification SF^+ (resp. relaxation SF^-) has a moderate influence on thermaline structure and circulation: temperature decreases (resp. increases) by 1.5°C ; the SML deepens to 35 m (resp. shoals to 20 m; see Figs. 9a,f); the upwelling jet extension deepens and expands offshore ~ 80 km (resp. shoals and contracts inshore).

As for vertical velocities, their change for SF^+ is substantial with a 100% increase to $\sim 6\text{ m day}^{-1}$ (Fig. 9a) and the presence of upward velocities all the way to 18°W . A reduction of w during SF^- exists but it is more difficult to evaluate in Fig. 9f because the alongshore averaging sector is at the edge of the upwelling/large w patch (see Fig. 8d).

The inner shelf is typically defined as the region where the surface and bottom boundary layers are coalesced and the water column is fully mixed. The outer edge of the inner shelf is important dynamically and also for the ecosystem. Its location varies from 17.2°W at days 6–9 during SF^+ to 17.1°W at days 6–9 during SF^- .

c. SSUS-scale temporal evolutions

Quantities represented in Fig. 10 (SST, SML depth, w at the mixed layer base, and u , v at the ocean surface) are spatially averaged over BoxN (see section 2d, Fig. 1b) where upwelling dynamics is prevalent. Some findings presented above in relation to Fig. 9 are also visible in Fig. 10 (e.g., magnitude of changes in SST $\sim \pm 1.5^\circ\text{C}$) but the latter provides detailed insight in the system temporal responses, e.g., the precise SSUS-scale changes in SML depth (~ 3 m with an asymmetry between SF^+ and SF^- discussed below) or the major changes in surface velocity magnitude during the synoptic events. In agreement with the study of Gan and Allen (2002b), these

velocity changes are associated with important modifications in alongshore pressure gradient (not shown).

We note a clear distinction between SST, which seems still away from equilibrium state toward the end of SF^\pm (day 8) and all the other variables which exhibit plateaus between day 3 and 8, albeit less clearly so for u_{surf} and SML depth. This particularity reflects the long inertia of thermal exchange processes. In sensitivity runs with a longer synoptic intensification plateau (16 instead of 6 days for T_p) SST does not decrease after day 10. This is useful information on the time scale of the system thermal response, which is thus ~ 10 days. Momentum adjustments typically need ~ 1 inertial period T_f (2 days) and are therefore faster, as confirmed by Figs. 10d and 10e.

SST response is also specific in that the rate of change is larger during the spinup (peak reached in ~ 7 days) than during the spindown phase (near-return to climatology in ~ 12 days), particularly for SF^- . We will return to this point in sections 4d, 6, and 7. Also, note that the return to climatology of u_{surf} is ambiguous toward day 22 when a small downward trend is still visible. We interpret this as a consequence of the climatological wind evolution during the month of March (see Fig. 2e). Except for SML depth, intrinsic variability is systematically less than the forced response at its peak during SF^\pm .

d. Intensification–relaxation asymmetries and the net effect of synoptic wind events

Quantifying the asymmetries between intensification and relaxation is an important objective of this study because it provides useful insight into the rectification effects induced by synoptic variability of wind forcings (note that modeling studies have frequently been performed using monthly climatological forcing devoid any synopticity; e.g., Marchesiello et al. 2003; Penven et al. 2005).

The relative importance of the asymmetry \mathcal{R}_{SF} (see section 2f) is indicated for each variable plotted in Fig. 10. SST presents rather minor asymmetries that develop after the peaks of forcing anomalies (Fig. 10a). They concern the time of peak ocean anomaly (day 9 for intensification and day 10 for relaxation) and time to near-return to climatology (\sim day 20 and beyond day 22, respectively). The latter asymmetry is observed at late times when climatological air–sea heat fluxes have changed substantially (see Fig. 2e).

Despite noticeable SF^+ – SF^- asymmetries in SML depth anomaly (resp. $+2$ and -4 m), \mathcal{R}_{SF} remains limited (6%). This is because the SML depth synoptic anomalies are much smaller than the climatological signal ($SML_{SF^0} \sim 17$ m). Asymmetries in w_{SML} (3%) and u_{surf} (8%) are also limited. The largest SF^+ – SF^- asymmetry is found for meridional surface velocities whose anomalies are respectively 10 and 15 cm s^{-1} (see Fig. 10), which yields $\mathcal{R}_{SF} = -14\%$. Underlying processes are discussed in section 7.

In Fig. 11, we show the spatial structure of the $RES_{SF}(v)$ field at the ocean surface and that for a cross-shore vertical section (with some alongshore averaging, see section 2d). Between CV and 14.25°N , quasi-barotropic poleward residual currents with magnitude ~ 0.05 – 0.1 m s^{-1} are manifest. Their

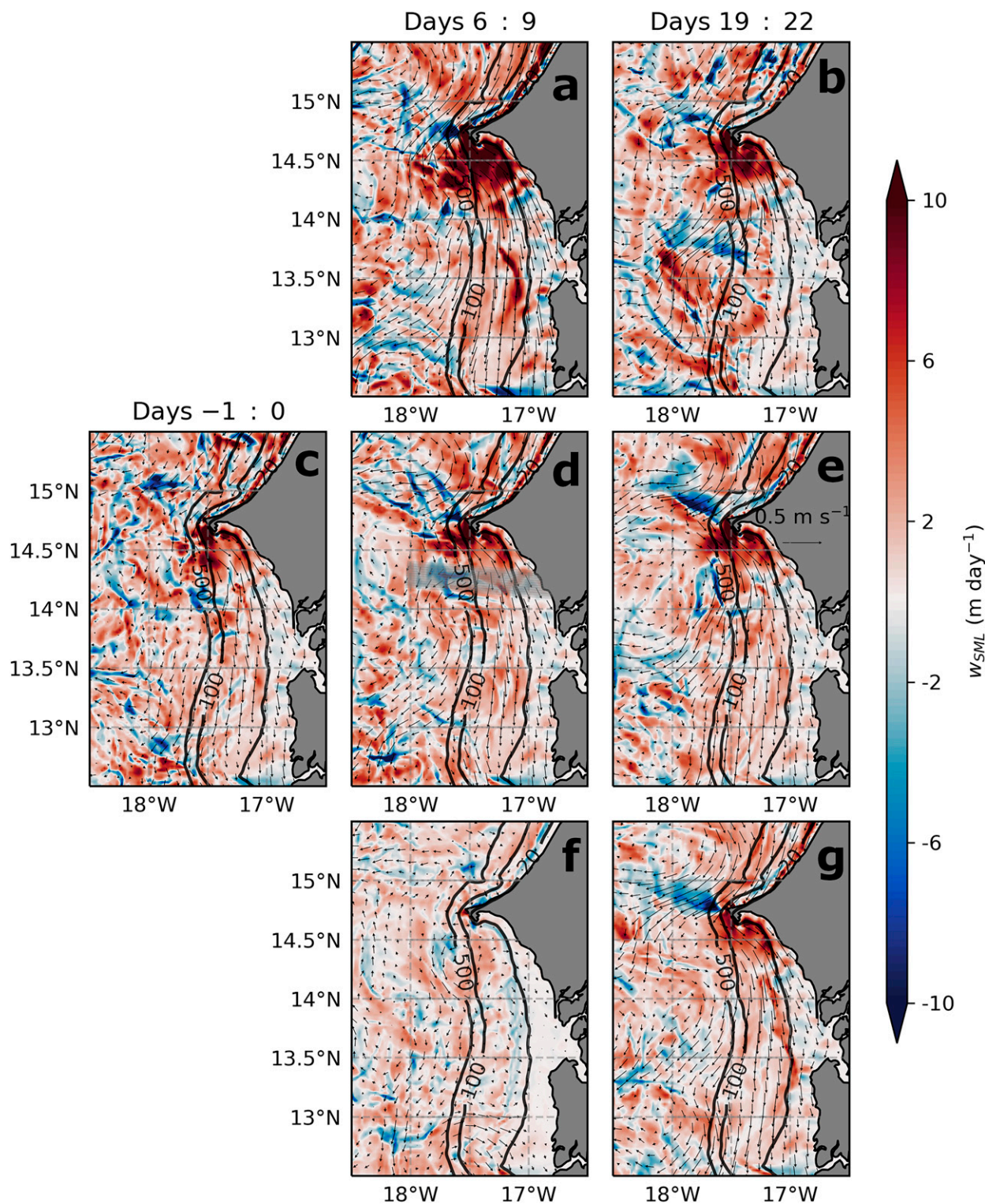


FIG. 8. As in Fig. 6, but for vertical velocities at the mixed layer depth.

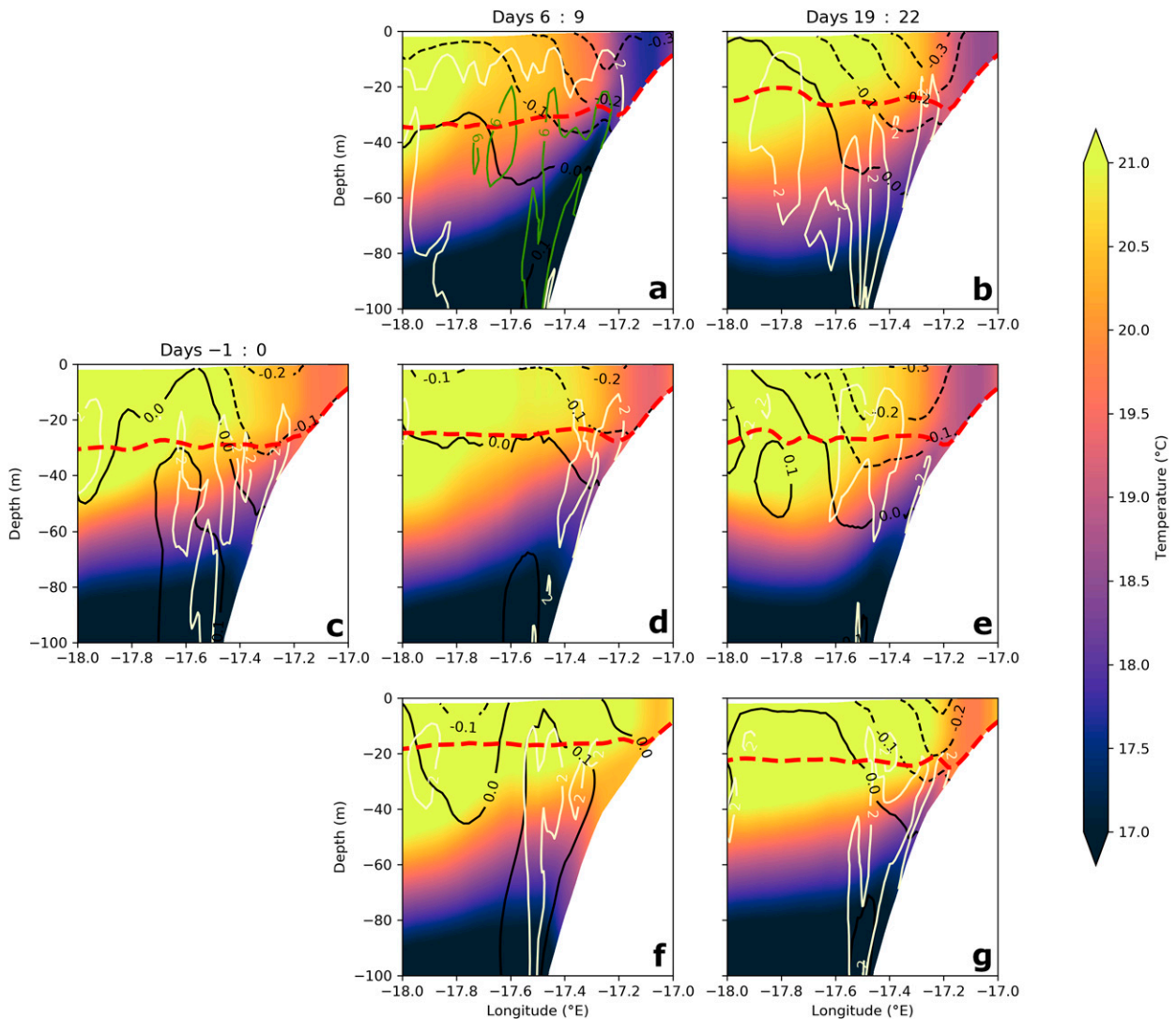


FIG. 9. Across-shore vertical section of temperature (color), surface mixed layer depth (red dashed line), meridional currents (black contours; m s^{-1}), and vertical velocities (white and green lines indicate isolines at 2 and 6 m day^{-1}). Fields are ensemble, alongshore, and time averaged. Alongshore averaging is carried out in the gray box represented in Fig. 7f using a regridding from longitude to ocean depth. (a),(b) SF^+ , (c)–(e) SF^0 , and (f),(g) SF^- evolutions are shown.

tendency is to oppose the southward climatological flow which improves the comparison with observations (section 3).

A more subtle class of asymmetries concerns the robustness of the ocean response (i.e., the relative importance of forced deterministic versus intrinsic response), which we describe for SST and SSH. During SF^+ intensification phase, SSH/SST patterns are robust over most of the shelf (excluding limited areas near the shelf break for SST) while this is only true for SSH during the SF^- relaxation phase. For SST, relaxation is associated with more ensemble run variability except over the inner shelf (cf. Figs. 7a,f). At later times ($t > \text{day } 9$), the robustness of the SSH patterns decreases more rapidly for SF^- than for SF^+ (Figs. 6a,b versus Figs. 6f,g). The evolution is opposite for SST (Figs. 7a,b versus Figs. 7f,g), i.e., the ocean response appears more deterministic for SF^- than for SF^+ , in agreement

with Fig. 3b. All this reveals the importance of intensifying winds (during the early part of SF^+ and the late part of SF^-) in deterministically organizing the SST field, and thus contribute to asymmetries.

e. Impact on the submesoscale variability

Frontal processes (i.e., submesoscales) have typical time scales of the order of a few days (McWilliams 2016). This is similar to the time scales associated with our synoptic fluctuations. Moreover, proximity to the coastline and rapid changes in bathymetry make identification of submesoscale through spatial filtering challenging. It is thus impractical to extract synoptic modulations of the submesoscale activity by applying spatiotemporal filters on quantities like density or lateral velocities, e.g., as done in Capet et al. (2008b). Instead, we

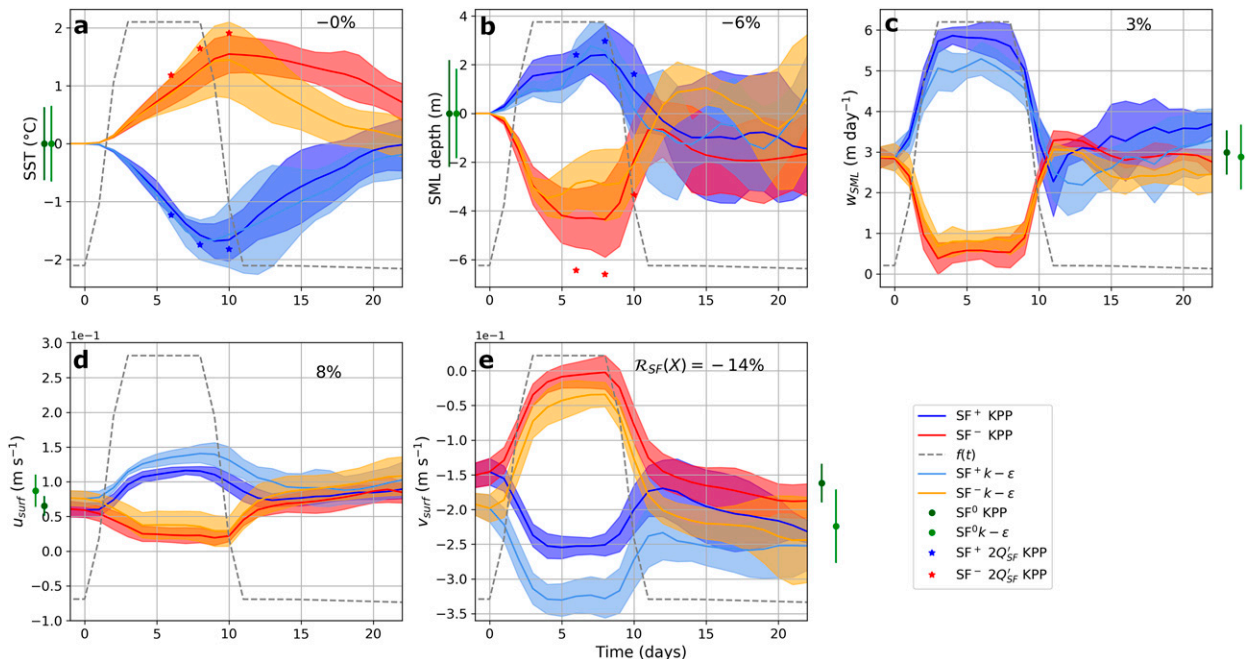


FIG. 10. Time series of (a) SST anomaly, (b) SML depth anomaly, (c) vertical velocity at the base of the SML, (d) surface zonal, and (e) meridional velocity for SF^+ and SF^- runs. Variables are ensemble and spatially averaged (over BoxN; see Fig. 1b). Blue (resp. red) lines correspond to SF^+ (resp. SF^-). Dark (resp. light) tones are for KPP (resp. GLS $k-\epsilon$) ensembles. Anomalies are relative to SF^0 . Red and blue stars in (a) and (b) indicate values found at days 6, 8, and 10 for the simulations forced with double heat flux anomalies ($2Q'_{SF}$). Green dots and bars left or right of the figure box represent respectively the averages and the intrinsic variability levels computed as plus/minus the maximum standard deviation (std) between day -1 and day 22 in the ensemble run SF^0 . Dark (resp. light) green is for simulations with KPP (resp. GLS $k-\epsilon$) turbulence submodel. Shaded envelopes represent the standard deviation computed each day from the different ensemble members. The gray dotted line represents the shape of the synoptic forcing anomaly [i.e., $f(t)$; see section 2c]. Percentages in the upper-right corner of each panel indicate the relative importance of the asymmetry between SF^+ and SF^- , $R_{SF}(X)$ (see definition in section 2f). Note that the amplitude of the y-axis range is similar in (d) and (e).

diagnose the RMS vertical velocities w_{SML}^{RMS} , a well-known faithful indicator of submesoscale (Lévy et al. 2001; Lapeyre and Klein 2006; Capet et al. 2008b). This quantity is computed over the southern box (see BoxS in Fig. 1b). Excluding the northern part of the SSUS ensures that upwelling vertical velocities are absent so that w_{SML}^{RMS} is considered a proxy for submesoscale turbulence. The strength of surface fronts and submesoscale activity is generally enhanced when conditions favor intense baroclinic instability, i.e., in the presence of strong regional-scale density contrasts and, most importantly, of deep SML (Fox-Kemper et al. 2008). This is also true over continental shelves, except for their shallowest part where bottom friction damps submesoscales very effectively [Capet et al. (2008a); see also Hetland (2017) and Kobashi and Hetland (2020) in the context of river plumes].

A reduction $\sim -30\%$ of w_{SML}^{RMS} is observed during SF^- (the small initial increase at days 0–3 also found in SF^0 is not considered statistically meaningful). Conversely, submesoscale activity is increased by $\sim 20\%$ during SF^+ compared to climatological conditions (Fig. 12a). Even larger departures are found at later times with a peak $\sim +100\%$ at day 15 and w_{SML}^{RMS} significantly above the climatological values until day 22.

The early part is consistent with changes in SML depth but the later part is not. Examination of w_{SML} fields at day 15 of individual runs reveals an alternating positive–negative w pattern, as typically associated with frontal intensification by mesoscale stirring (Wang 1993). It is moreover systematically located at the northern edge of the mesoscale cyclone described in section 4a and thus intimately tied to the lateral offshore export of cold upwelling water that follows SF^+ . Likewise, the weaker cyclone produced during SF^- also leads to enhanced w_{SML} in its vicinity, albeit with less sharp structures. All this illustrates the subtlety of the relationships between forcings and fine-scale coastal ocean response, and in particular the possible existence of time lags of a few days between their respective evolutions. Another subtlety concerns the apparent SSUS scale decoupling between the evolutions of w_{SML}^{RMS} and $|\nabla_{hp}|$ (cf. Figs. 12a and 12b). We attribute this to the overwhelming importance of temperature contrasts in the inshore band where friction inhibits the classical expression of frontogenesis. Specifically, we find that, in BoxS, averaged $|\nabla_{hp}|$ is ~ 3 times stronger inshore of the 15 m isobath compared to offshore. The heat budget analysis presented below adds further support to the fact that, despite the noticeable

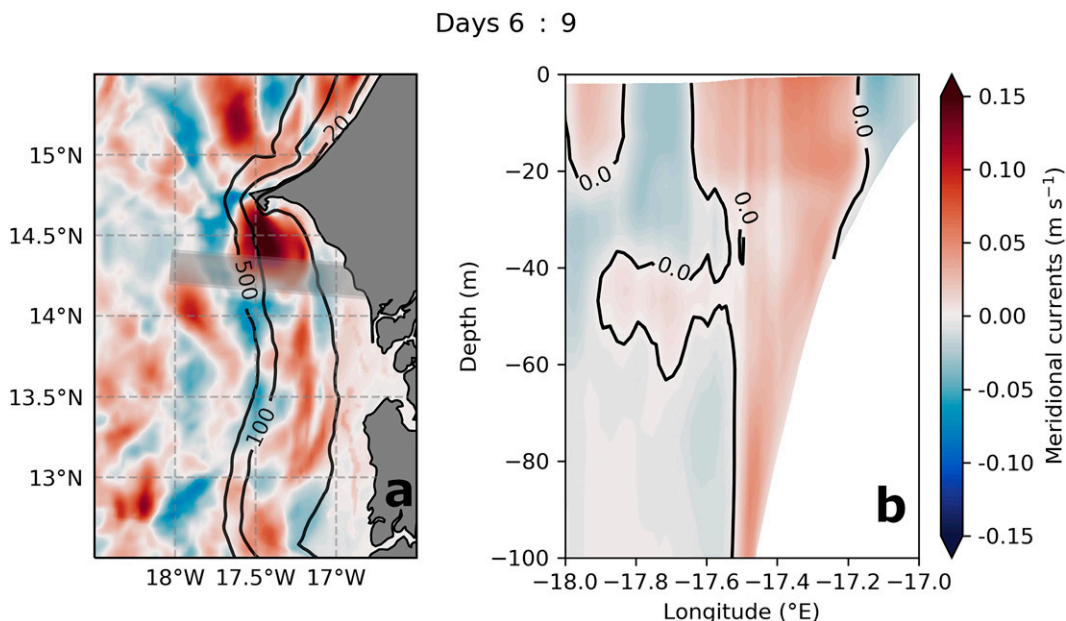


FIG. 11. (a) Surface slice and (b) vertical-across-shore section of ensemble, alongshore, and time averaged meridional current residual $RES_{SF}(v)$ (see definition in section 4d). Time (resp. alongshore) averaging is performed between days 6 and 9 included [resp. over the sector shaded in gray in (a)].

response of w_{SML}^{RMS} after SF^+ , the modulation of SSUS submesoscale by synoptic events is modest.

5. Mixed layer heat budget

Considering the vertical velocities, surface current and SST patterns, we hypothesize that the northern part of the shelf (BoxN in Fig. 1b) is the preferential location where upwelling of cold waters occurs (Ndoye et al. 2017). To qualify this and

more generally gain insight into the respective roles of the different processes in warming/cooling during synoptic events, we carry out a SML heat budget (see section 2g) over various areas of the shelf. In all simulations (SF^+ and SF^0), vertical mixing and entrainment are of secondary importance. Our focus is thus on air–sea heat exchanges (FORC), advection terms ($ADV = HADV + VADV$), and the heat rate of change (RATE) which is approximately equal to the sum.

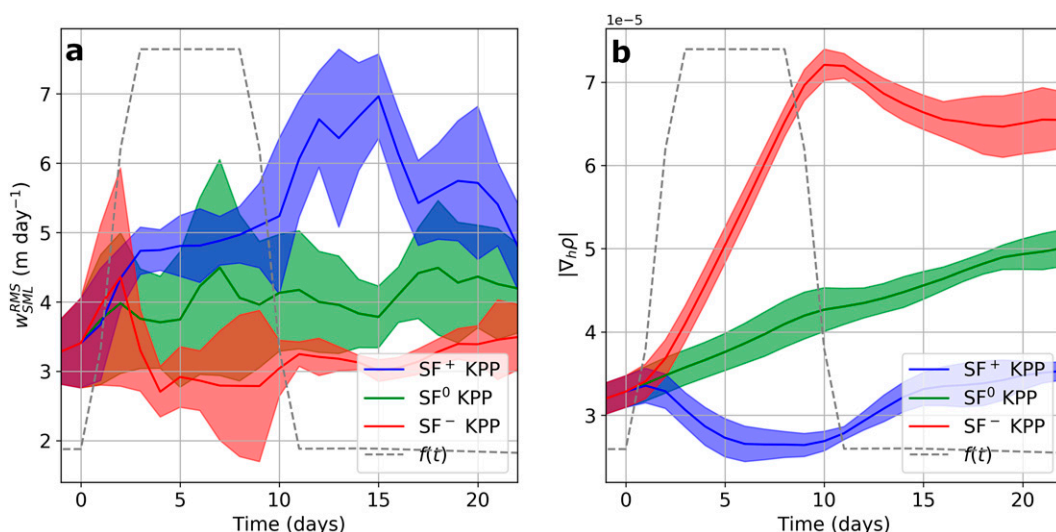


FIG. 12. (a) Vertical velocities at the base of the SML. (b) Horizontal density gradient magnitude $|\nabla_h \rho|$. Both quantities are averaged over BoxS (see Fig. 1b) and represented for SF^+ (blue), SF^0 (green), and SF^- (red). Shaded envelopes indicate the ensemble standard deviation.

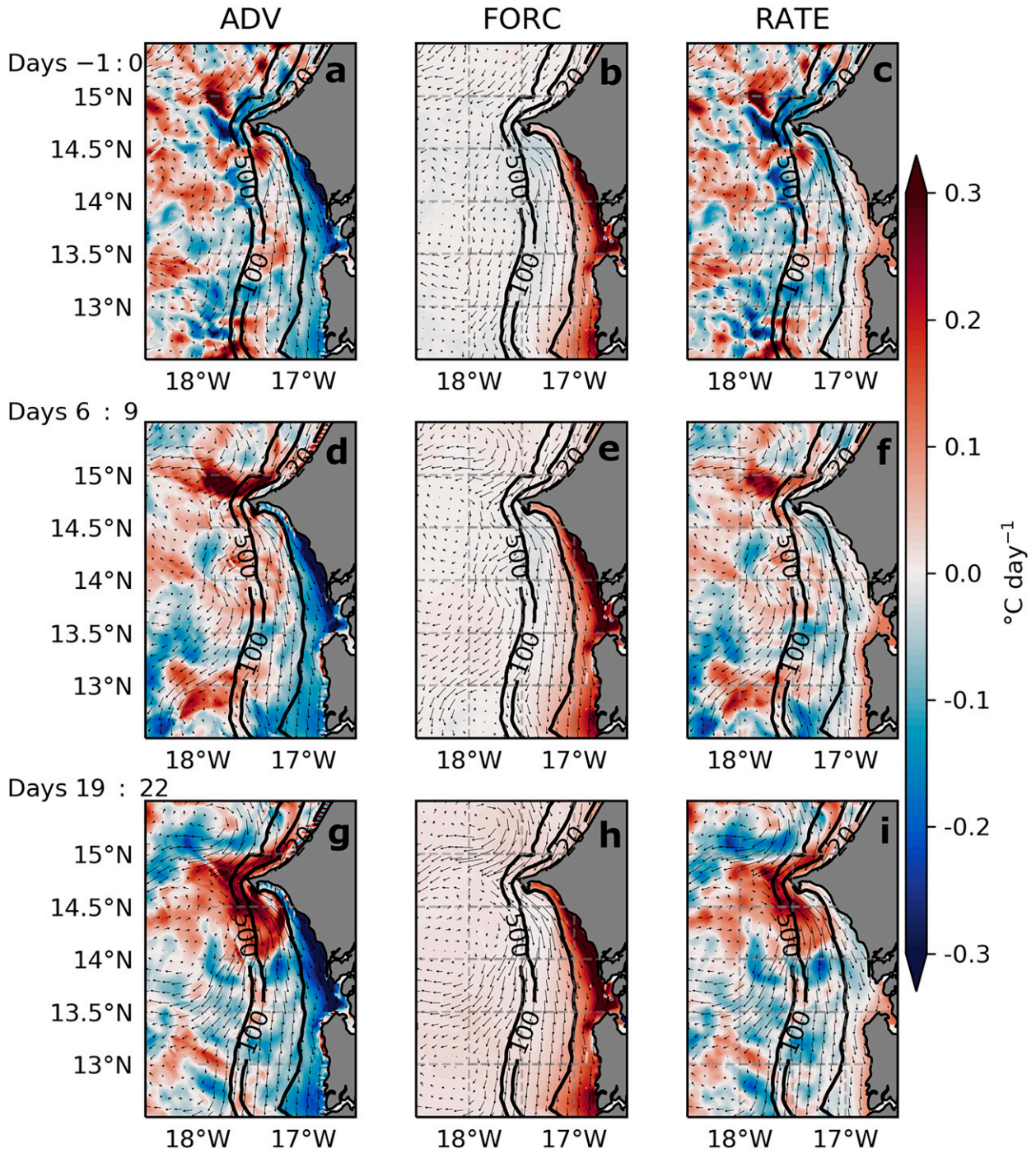


FIG. 13. (left) Ensemble averaged SF^0 advection, (center) atmospheric forcing, and (right) heating rate terms as defined in Eq. (9) ($^{\circ}\text{C day}^{-1}$). Surface velocities are also shown (arrows). The three rows are for the same three time windows used in Figs. 6 and 7: (a)–(c) from days –1 to 0, (d)–(f) days 6–9, and (g)–(i) days 19–22.

a. Spatial structure

Figures 13–15 show FORC, ADV, and RATE for SF^0 , SF^+ , and SF^- , respectively. In all three cases, the inner shelf is characterized by robust FORC (resp. ADV) warming (resp.

cooling) contributions, albeit less so for SF^+ (resp. SF^- , note the weak warming patch between 13.5° and 14°N for days 6–9, see Fig. 15a). This contrasts with the situation found over the mid and outer shelf where tendency terms are uniformly small (FORC) or spatially variable (ADV). The FORC warming

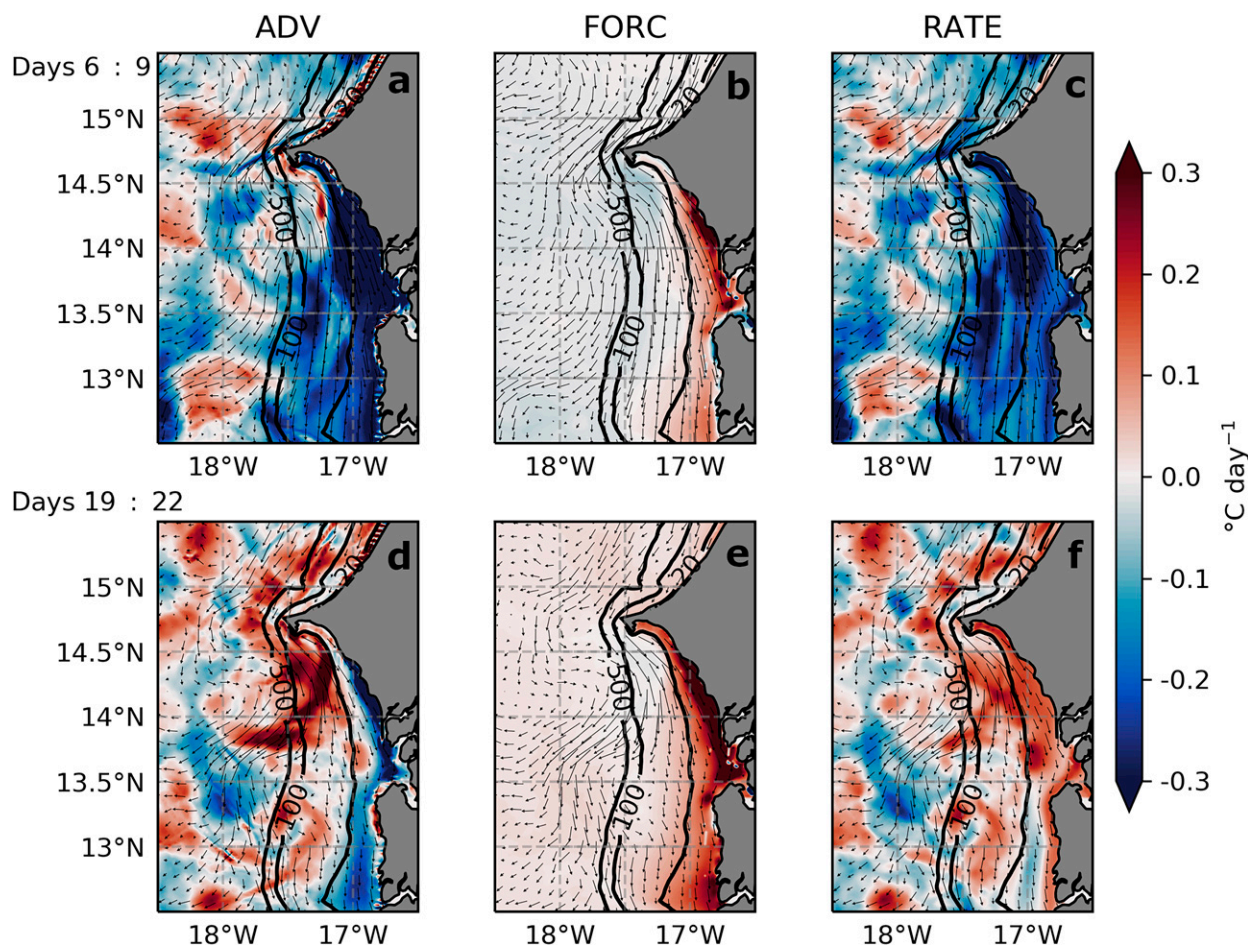


FIG. 14. As in Fig. 13, but for SF^+ . Averages over the time window before the synoptic anomaly (from days -1 to 0) is as for SF^0 and is therefore not repeated (see Figs. 13a–c).

pattern is due to the spatial structure of the air–sea heat flux forcing field (not shown), and not to spatial differences in how shortwave heat flux is distributed vertically between the mixed layer and the subsurface. Note that nearshore air–sea heat flux warming arises from the SST bias correction terms m_2 and m_{2adj} present in Eq. (A4). Our experience at sea in the region suggests that this may be a realistic feature associated with coastal wind drop off that is absent in existing wind reanalyses products, not accounted for in large scale air–sea heat flux products such as ICOADS used in m_1 , but recovered thanks to the bias correction terms.

During the intensification part of SF^+ , FORC is, by construction, reduced compared to climatological conditions (see Fig. 2b). However, the cooling tendency observed in RATE at days 6–9 is dominated by changes in ADV, which becomes strongly negative over most of the shelf. After the intensification, ADV cooling is restricted to a small inshore portion of the shelf while ADV warming has a small influence on the heat budget between 13.5° and 14.75°N . However, this warming tendency at days 19–22 is also found in SF^0 , and to a lesser extent SF^- (in which the latitudinal extent of the warming

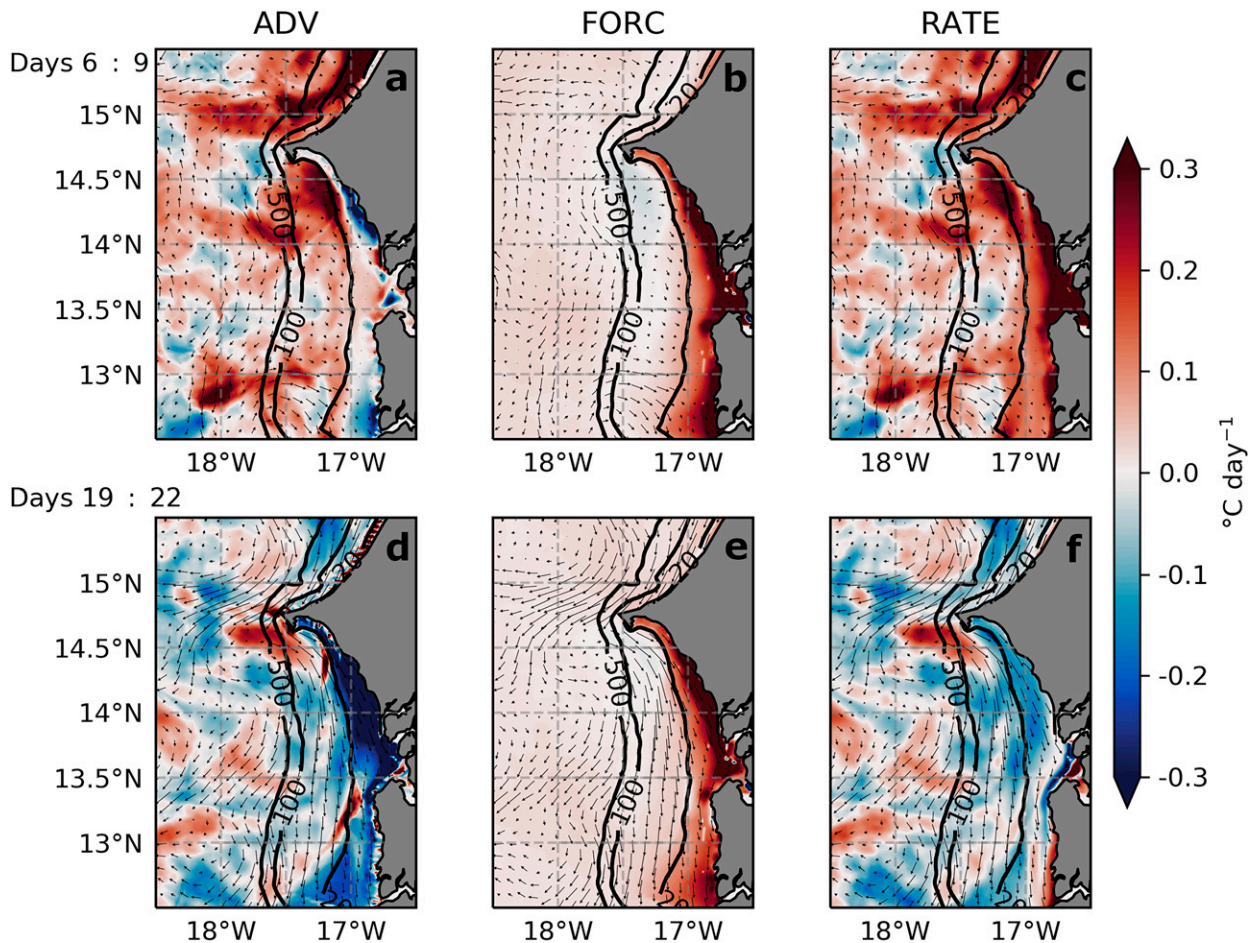
patch is much reduced). Thus, this warming pattern in SF^+ reflects not only a postsynoptic event adjustment but also the spring seasonal warming trend present in the climatology of air–sea heat fluxes (Fig. 2e).

During the relaxation, advection brings heat over most of the shelf except for a tiny inshore sector (Fig. 15a, 14° – 14.6°N) where ADV cooling persists. There, the SML is strongly warmed by the atmospheric forcing (Figs. 15b,e). When the relaxation stops, heating from the atmosphere slightly decreases but advection is the dominant cooling driver (Fig. 15d) that brings SML temperature back to climatological conditions.

A contribution due to restratification by submesoscales is presumably hidden in ADV (except over the inner shelf where frontal processes are strongly damped). But we do not find any indication that it differs between SF^+ and SF^- , in agreement with the modest response of the submesoscale presented in section 4e.

b. Box averaged heat budget

A more in-depth analysis is now given thanks to horizontal averaging, introduction of a reference temperature T_0 , and

FIG. 15. As in Fig. 14, but for SF^- .

separation of the horizontal versus vertical advection terms (see section 2g). First, averaging of the SML heat budget terms is done over the northern part of the shelf (BoxN in Fig. 1b). We start with SF^0 in which RATE is consistent with expectations (positive and increasing slightly over time, Fig. 16a) but the relative contributions of lateral and vertical advection appear counterintuitive for an upwelling region. Indeed, we find that lateral advection tends to cool the SML ($\sim -0.1^{\circ}\text{C day}^{-1}$) while vertical advection is nearly zero.

During the intensification period of SF^+ (Fig. 16b), the same general remark applies although horizontal advection cooling is intensified (to $\sim -0.2^{\circ}\text{C day}^{-1}$) and vertical advection is weakly (but robustly) negative ($\sim -0.05^{\circ}\text{C day}^{-1}$). Overall, RATE is dominated by HADV between days 3 and 8.

SML warming (RATE) changes rapidly toward the end of the intensification period and reaches $+0.2^{\circ}\text{C day}^{-1}$ at day 11. An oscillatory behavior is manifest at later times. It is due to HADV and partly compensated by VADV. Examination of the lateral heat transport anomalies at the boundaries of BoxN with the help of the PAGO software (Deshayes et al. 2014; Barrier et al. 2015) (available at

<http://pypago.nicolasbarrier.fr/>) reveals synoptic modulations in the relative rates of warm water ($T > T_0$) import into and export out of BoxN. Import predominantly takes place through the northern part of the offshore boundary, whereas export predominantly takes place through the southern part of the offshore boundary and through the southern boundary (not shown). Both import and export of heat are impacted by the evolutions of the mesoscale eddy field described in section 4a, which gives rise to the oscillations of RATE observed after the wind intensification period.

In first approximation, SML heat content modulation during SF^- are opposite to those found in SF^+ : increasing HADV and VADV during the relaxation part; rapid return to negative HADV around day 9–11; reduced magnitude of VADV compared to HADV. On the other hand, close examination reveals some differences in behavior: a change in the sign of VADV at day 6; relative weakness of the oscillations that follow the relaxation phase compared to those seen after the intensification in SF^+ ; differences in RATE and HADV extrema during active part of SF^+ ($-0.3^{\circ}\text{C day}^{-1}$ for RATE) and SF^- ($+0.2^{\circ}\text{C day}^{-1}$ for RATE); increase in intrinsic variability observed between days 5 and 10 (i.e., toward the

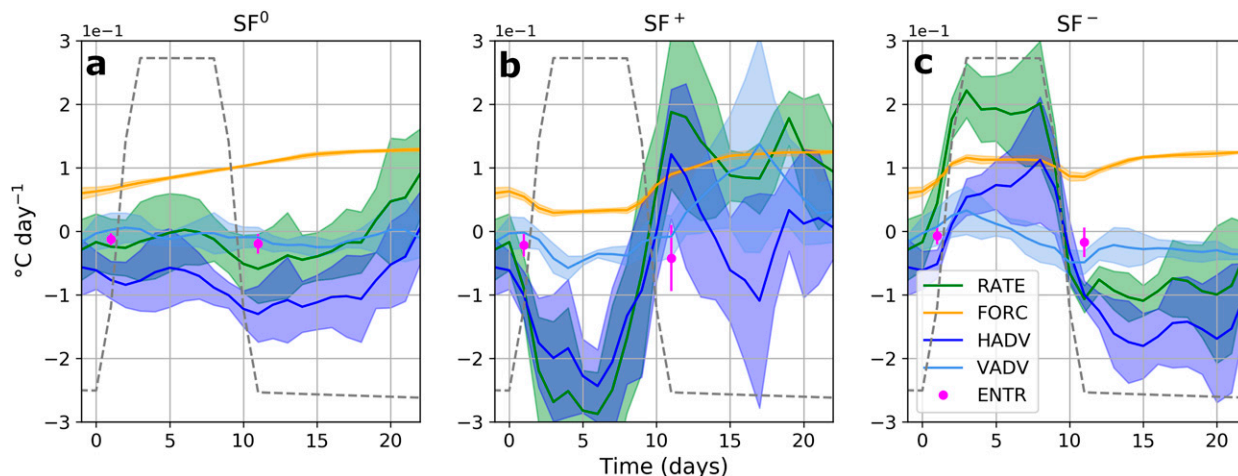


FIG. 16. (a)–(c) Time series of ensemble and BoxN (see Fig. 1b) spatially averaged heat budget tendency terms. Color coding of the different terms is indicated in (c). Shaded envelopes represent the ensemble standard deviation. Panels (a), (b), and (c) correspond respectively to SF^0 , SF^+ , and SF^- . Magenta dots located at $t = 1$ day (resp. $t = 11$ days) provide entrainment (ENTR) values time averaged between day 0 and 9 (resp. between day 10 and 22). The associated magenta bar represents the maximum value of the ensemble standard deviation over the corresponding time window.

end of the relaxation period) versus between days 8 and 12 in SF^+ .

The surprisingly small role played by vertical advection (Figs. 16a–c) deserves further elaboration. To the readers familiar with more energetic upwelling sectors, e.g., offshore of central California or Chile, we remind that vertical velocities are weak in the SSUS, typically a few meters per day [see Fig. 8 and also discussion in Capet et al. (2017)], and do not dramatically increase with strong winds. This being said, the shape of the SSUS upwelling tongue (Fig. 7) and the fact that the Cape Verde Peninsula is effective at interrupting the along-shore flow of cold upwelling water strongly suggests that a heat sink (i.e., a source of cold water) must cool the SML south of Dakar. To confirm this and estimate the importance of this sink, we perform heat budget analyses for several BoxN-like control domains that differ by the latitude (lat) of their southern edge, varied from 13.5° to 14.5° N with 0.25° increments. The northern and offshore edges of the control volumes remain fixed at 14.75° N and at the 100-m isobath respectively, as for BoxN. These boxes are designated by S_{lat} (so that BoxN is S_{14}) and their area is denoted S_{lat} . HADV and VADV contributions to the heat budget equation are denoted with a subscript lat and represented as a function of control volume extension in Fig. 17.

VADV cooling is important in SF^+ and SF^0 but it is very concentrated in the northernmost part of the SSUS ($-0.1^\circ\text{C day}^{-1}$ in $S_{14.5}$ for SF^+), where HADV is, conversely, a heat source (SF^- and SF^0) or negligible heat sink (SF^+). As the domain extension increases southward the magnitude of the VADV (resp. HADV) contribution is reduced (resp., increased). Precisely, HADV becomes dominant between 14.25° and 14.5° N. The negligible role of VADV cooling occurring south of 14.5° N in SF^+ is demonstrated by comparing its mean effect in $S_{14.25}$ and S_{14} to the effect obtained by “diluting” the VADV contribution in $S_{14.5}$. Precisely Fig. 17

shows $VADV_{14.5} \times (S_{14.5}/S_{14.25})$. A minor contribution of VADV is still present between 14.25° and 14.5° N but most of the cooling in $S_{14.25}$ (82%) actually takes place in the northernmost ocean sector $S_{14.5}$. Because $VADV_{14.5} \times (S_{14.5}/S_{14.0}) < VADV_{14}$, we infer that vertical advection must overall warm the SML between 14.25° and 14° N (with an absolute magnitude equal to 25% of the cooling found in $S_{14.25}$). South of 14° N changes become small except for the role of HADV during SF^+ which keeps decreasing all the way to 13.50° N, reflecting the southward expansion of the upwelling tongue.

In the northern part of the SSUS, VADV is found to have a significant warming contribution in SF^- . Despite the limited role of frontal processes in our SSUS simulations (section 4e) we see this as evidence of baroclinic instability processes, i.e., of correlations between temperature and vertical velocity fluctuations.

Figure 17 also reveals the asymmetric roles played by lateral and vertical advection. The largest $RES_{SF}(VADV)$ value is found in the smallest northern box where SF^+ (resp. SF^-) has little (resp. a large) effect on VADV compared to the climatological reference (see Fig. 17b). HADV asymmetry is distinct in behavior but also decreases as the control volume gets bigger. A modest level of asymmetry is found for $S_{13.5}$. This is in apparent contrast with the results of Send et al. (1987) but consistent with the importance of alongshore heat advection in the SSUS, even during sustained upwelling conditions. Overall, our analysis demonstrates that asymmetry and rectification are strongly domain dependent.

These findings are in part dependent on the choices made when designing the idealized forcings and in particular the magnitude of air–sea heat flux anomalies (section 2c), i.e., they reflect moderate amplitude springtime synoptic events (see section 7 for further elaboration).

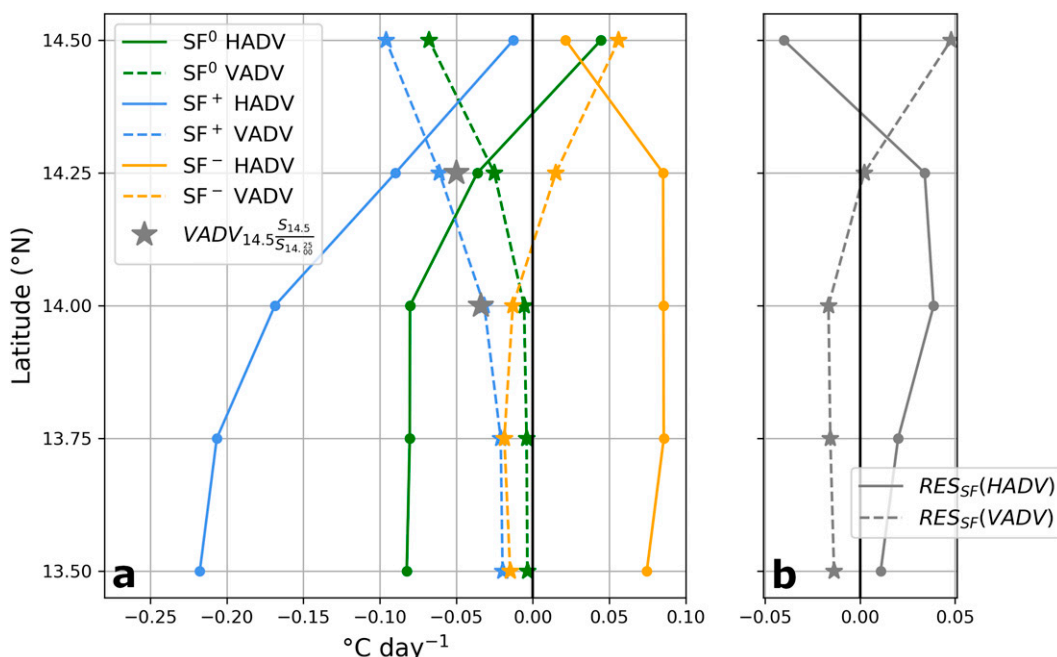


FIG. 17. (a) Horizontal (solid lines) and vertical (dashed lines) heat advection tendencies as a function of the location of the averaging box southern boundary (which varies from 13.50° to 14.50°N). Five averaging boxes are used (indicated with dots and stars superimposed on lines). Each tendency value is ensemble and time averaged (between days 6 and 9, i.e., at the end of the synoptic anomaly if any). Green, blue, and orange lines indicate respectively SF⁰, SF⁺, and SF⁻. Isolated gray stars represent the outcome of diluting the SF⁺ vertical advection tendency found north of 14.50°N in the boxes with southern extension at 14.25° and 14.00°N. (b) SF⁺/SF⁻ asymmetry (i.e., synoptic residual) RES_{SF}(X) associated with the domain-averaged horizontal (solid) and vertical (dashed) advection tendency terms shown in (a).

6. Sensitivity tests and limitations

a. Vertical mixing scheme

Previous studies have shown the sensitivity of coastal dynamics to the particular choice made for the turbulence closure scheme (Wijesekera et al. 2003; Van Roekel et al. 2018). Here we explore this sensitivity by comparing the reference simulations using *K*-profile parameterization (Large et al. 1994) with simulations computed with the generic length scale (GLS) *k*- ϵ (Fearon et al. 2020; Umlauf and Burchard 2003). GLS *k*- ϵ surface mixed layer depths (computed using a threshold condition on density change from surface to mixed layer base equal to 0.01 kg m⁻³; see de Boyer Montégut et al. 2004) tend to be smaller (~2 m, not shown) than those obtained when using KPP.

The synoptic anomalies of SML depth generated by both schemes are quite similar for SF⁺. The differences are more pronounced for SF⁻, with less shoaling (resp. more deepening) during the active part (resp. the return to climatological conditions) when using GLS *k*- ϵ . From this ensues visible differences in SST during the late period of SF⁻ when GLS *k*- ϵ yields a faster return to climatological SST values (Fig. 10a).

The most dramatic sensitivity is found for zonal and meridional currents. The currents are systematically weaker with KPP than with GLS *k*- ϵ and the difference is amplified as wind (and currents) get stronger (Figs. 10d,e). The treatment

of bottom friction is identical in all runs (linear drag with friction coefficient equal to 3×10^{-4} m s⁻¹). We thus attribute this sensitivity to differences in momentum mixing intensity and indeed have verified that KPP yields viscosity coefficients near the shelf bottom that are 3–5 times stronger than found in GLS *k*- ϵ (differences over the inner shelf are even more pronounced). Although changing the vertical mixing scheme does not fundamentally alter our results, exploring this sensitivity further and determining which scheme is most realistic would be useful (but note that the flow bias at Melax shown in section 3a would be even stronger with GLS *k*- ϵ).

b. Doubling air–sea heat flux synoptic anomalies Q'_{SF}

As in other upwelling systems (Thomsen et al. 2021), net air–sea heat flux is quite variable at synoptic and intraseasonal time scales in the SSUS (e.g., at Melax; S. Faye 2016, personal communication). To explore this sensitivity, simulations with doubled Q'_{SF} (± 80 W m⁻² in SF⁺) were carried out. In terms of magnitude, sensitivity of SST is moderate [+10% (resp. 30%) SST anomaly at day 8 in SF⁺ (resp. SF⁻); Fig. 10a] and that of SML depth is a bit stronger [+25% (resp. 50%) SML depth anomaly at day 8 in SF⁺ (resp. SF⁻); Fig. 10b].

The asymmetry found between SF⁺ and SF⁻ is consistent with the fact that thermodynamic effects are amplified when the momentum forcing (wind) is weak. But overall, these sensitivity runs confirm that wind forcing is the dominant driver.

A different conclusion would presumably be reached for isolated synoptic events taking place in November–January when easterly winds from the Sahara can be responsible for Q'_{SF} anomalies reaching several hundred watts per square meter (Thomsen et al. 2021).

c. Study limitations

There are several important limitations to the insight provided by our study. First, the idealizations we made ignore the complexity of the wind and air–sea heat flux history (succession of synoptic events of various duration and intensity) and of the associated ocean response.

It has been known for a long time that coastal upwelling can be generated by remote winds whose effect is then transmitted (poleward along an eastern boundary) by coastal trapped waves (Philander and Yoon 1982). Synoptic wind anomalies have a regional imprint (Fig. 2c) which is very weak south of 12°N, i.e., our domain of interest is close to the southern limit of the synoptic fluctuation pattern. Consistently, we find very limited signs of propagation of remote synoptic signals in the SSUS (e.g., in v_{surf} and SSH) but this may be otherwise for some of the real world synoptic events. Using climatological boundary conditions for all runs, we also ignore the synoptic modulations of the West African Boundary Current (WABC) system that are generated outside our computation domain (i.e., remote forcing south of ~6°N). SSH altimeter data (Polo et al. 2008) and tropical Atlantic simulations (Polo et al. 2008; Kounta Diop 2019) indicate that coastal trapped waves generated by seasonal and intraseasonal wind fluctuations along West Africa can propagate from as far as the Gulf of Guinea to the SSUS.

Also note that we suspect a spring bias in the intensity of the WABC based on SST/ocean color satellite image analyses (Ndoye et al. 2014), but lack current observations to confirm this. Having an overly weak poleward WABC could limit the ability of wind relaxations to trigger continental shelf flow reversals (Tall et al. 2021) and thus also explain the flow bias at Melax (see section 3a). Finally, spatial horizontal resolution is only marginally submesoscale permitting (Dong et al. 2020), so frontal processes must be less energetic in our model than in the real ocean, which could have consequences on the SML heat budget and its synoptic modulations.

7. Discussion

Cape Verde is a major geomorphological irregularity with implications on the surrounding ocean flow. As shown in Gan and Allen (2002b), we also find that alongshore pressure gradients tend to be of opposite sign north and south of the Cape. On the other hand, the details of the circulation differ from those presented for the well-studied Point Reyes, Point Arena (Gan and Allen 2002b), and Cape Blanco (Barth et al. 2000).

In the typology established by Largier (2020) the SSUS geometry/flow configuration would fall in between two categories relevant to other ocean sectors: (i) smooth and broad embayment with no flow separation (e.g., Sonoma Coast in California and Antofagasta Bay in Chile) and (ii) abrupt coastline deflection associated with a flow separation and shelf recirculation (e.g.,

Gulf of Farallones in California and St Helena Bay in South Africa). Although Cape Verde also seems rather sharp, and a flow separation is manifest (Fig. 6), no recirculation occurs in normal/climatological conditions. In the model simulations we presented, this remains true during strong upwelling and relaxation conditions, albeit with some robust flow modifications induced in part by mesoscale features. We attribute this relative stability of the flow to the strong constraint associated with the shelf enlargement south of Cape Verde and to the associated onshore flow needed to satisfy the mass balance (Pringle 2002).

One manifestation of this stability is the importance of the deterministic response to forcing synoptic modulations relative to intrinsic turbulent variability. SSUS flow modifications generated when the system is subjected to upwelling wind intensifications or relaxations are indeed largely independent of the initial state at onset of the synoptic event. To leading order, they are also spatially homogeneous over the continental shelf. As for time scales, our analyses of synoptic modulation and return to climatological conditions demonstrate that the SSUS circulation and dynamics is constrained by the forcing history over a relatively short period of ~10 days (see Fig. 3a), i.e., memory effects are quite limited in time. Both the persistence in time of SF effects and the spatial heterogeneity of the ocean response to SF are significantly bigger for the open ocean (not shown). All this is consistent with the prevalence of a wind-forcing bottom friction balance in the momentum equations.

Given the design of our experiments, any asymmetry between the ocean response to SF^+ and SF^- forcing anomalies provides insight into residual effects generated by wind synoptic variability. Diagnosed asymmetries (Figs. 10 and 11) are small for SST, SML depth, w at the mixed layer base and a bit stronger for currents, particularly meridional ones. In the spirit of Gan and Allen (2002b) the possibility that alongshore pressure gradients at the offshore edge of our domain be responsible for asymmetry found for the latter was examined. Alongshore sea level gradient diagnosed over the 100 m isobath between 14° and 14.6°N reveal negligible asymmetry [$\mathcal{R}_{\text{SF}}(X) = 3\%$, not shown]. Reasons underlying asymmetry in v were not explored further given their limited importance overall. Bottom drag which was chosen to have a linear formulation cannot produce asymmetries alone but its interplay with near-bottom mixing could. Note that more asymmetry would presumably arise from employing quadratic/nonlinear bottom drag.

The intriguing SST asymmetry taking place after the period of anomalous synoptic forcing (Fig. 10) is sensitive to the employed mixing scheme. The longer persistence of SST and SML depth anomalies with KPP mixing may point to erroneous hysteresis effects but a more in-depth investigation would be needed to confirm this.

A well-known source of asymmetry is thermal/density advection in the bottom boundary layer which behaves differently in upwelling and downwelling conditions (Beckmann 1998). Because we find little asymmetry in bottom temperature/density, as estimated using the synoptic residual RES_{SF} (not shown), the importance of this effect must also be small.

The reader familiar with the California Current literature may be surprised by the limited asymmetry revealed by our surface mixed layer heat budgets. We relate this to the importance of alongshore advection, not just during relaxation but also during sustained wind conditions. This may be due to the shelf flow regime and its control by friction. Also note that we find significant asymmetry of the vertical and horizontal advection terms for the northern part of the SSUS, i.e., a control volume of size not much smaller than the one considered by Send et al. (1987). This underscores the domain dependence of synoptic rectification effects.

The degree to which the circulation responds deterministically is also noticeably different between SF^+ and SF^- , with significantly more robust SST responses in the former case as long as the synoptic wind anomaly is present (cf. Figs. 7a,f; see also Fig. 3b until day 11). This is perhaps not unsurprising that stronger forcing is associated with larger signal to noise, but it has, to our knowledge, not been noted before in this context. At later times when the wind has returned to climatological conditions, the opposite is true (cf. Figs. 7b,g; see also Fig. 3b after day 11), which seems consistent with more energy being available in SF^+ to feed turbulent processes.

8. Conclusions

In this study we shed light into the upper-ocean SSUS heat balance. At the time of year we focus on (the heart of the upwelling season) air–sea heat flux is the only significant source of heat. This heat input compensates cooling by advection which arises from the horizontal flow except in the immediate vicinity south of Cape Verde where vertical advection dominates. All this is broadly consistent with the localization of vertical velocities found in Ndoye et al. (2017) (see also Fig. 8).

However, the main study focus is the effect of atmospheric fluctuation in the synoptic range. In upwelling systems, such fluctuations can strongly modulate the ocean dynamics and have been implicated in anomalous biogeochemical events of high significance.³ By means of idealized ensemble runs we have strived to characterize the ocean response of a West African upwelling sector to atmospheric synoptic fluctuations.

During upwelling intensification the dominant SSUS upwelling pathway identified in climatological conditions (Ndoye et al. 2017) remains in place and most of the upwelling takes place within 20–30 km from the Cape Verde Peninsula. During wind relaxations, upwelling is nearly halted (although the wind is not) and the horizontal flow is modified with weak equatorward currents over the shelf and even surface poleward flow about the shelf break. The associated changes in SST (or mixed layer temperature) are smooth in time, spatially modulated by (sub)mesoscale turbulence with magnitude reaching $\pm 1.5^\circ\text{C}$. The synoptic modulations of the underlying heat budget are characterized by major disruptions of the heat tendency terms with a near doubling (resp. complete reversal) of the horizontal and vertical advection tendency terms north

of 14.25°N during SF^+ (resp. SF^-). Air–sea heat fluxes are comparatively less affected although they also play a role.

Overall, we confirm the major role played by horizontal advection in the SSUS upper-ocean heat balance and its changes on synoptic time scales (Capet et al. 2017). Conversely, we find a very limited role played by vertical mixing. Our analyses also demonstrate the existence of modest intensification/relaxation asymmetries at the upwelling sector scale, i.e., the mean state dynamics and circulation of the SSUS are only weakly altered by the presence of synoptic scales in the atmospheric forcings. Of all dynamical variables considered, meridional velocities are subjected to the most important rectification effect. But, contrary to general expectations that could be derived from past studies (Gan and Allen 2002a,b, 2005a), no associated alongshore pressure gradient asymmetry could be identified in our simulations.

All these findings are for a particular class of synoptic perturbations whose magnitude is one standard deviation above or below climatology. This is sufficient to draw the ocean outside of its intrinsic variability range and produce major biogeochemical disturbances as we will report in a forthcoming study including substantial biogeochemical asymmetries. But stronger perturbations would presumably have stronger effects, and possibly increase the degree of asymmetry between upwelling intensification and relaxation phases. During the monsoon to upwelling transition season in fall, offshore wind carrying dry air from the Sahara and warm ocean temperatures lead to intense air–sea heat losses that make for very different synoptic situations, and perhaps more surface heat flux forcing asymmetry. Exploring the whole variety of synoptic circumstances may be tedious. Gaining a priori insight into which ones are most impactful on the biogeochemical and ecosystemic functioning (e.g., because they produce hypoxic or harmful algae bloom events) of the SSUS would be useful.

Acknowledgments. This work benefited from Agence nationale de la recherche fundings (SOLAB ANR-18-CE32-0009). P. C. was supported by a PhD grant from IPSL EUR. CROCO is provided by <http://www.croco-ocean.org>. Fundings for the Melax mooring were provided by FP7 PREFACE and IRD laboratoire mixte international ECLAIRS2. Simulations were performed using HPC resources from GENCI-IDRIS (project A0130101140).

Data availability statement. The ERA5 dataset provided by the ECMWF is available on <https://cds.climate.copernicus.eu/cdsapp#!/dataset/reanalysis-era5-single-levels?tab=overview>. Melax data can be requested on <https://sites.google.com/site/jointinternationallabeclairs/melax>. Given the large size of the modeling experiment outputs (~ 1.6 TB), the dataset is not stored online and can be shared upon request to the corresponding authors.

APPENDIX A

Net Heat Flux Forcing Implementation

As large uncertainties remain on local and regional heat fluxes, model climatological simulations are often performed

³ Away from shore, the existence of such events can also be purely due to mesoscale turbulence, which modulates the flow and biogeochemical properties over a similar time scale range (Stukel et al. 2017; Chabert et al. 2021).

using online SST restoring to correct for heat flux bias (e.g., Ndoye et al. 2017) using the formulation proposed by Barnier et al. (1995):

$$Q_{\text{climM}}(t) = \overbrace{Q_{\text{climO}}}^{(m_1)} + \overbrace{\frac{dQ}{d\text{SST}}[\text{SST}_{\text{onlineM}}(t) - \text{SST}_{\text{climO}}]}^{(m_2)}, \quad (\text{A1})$$

where $\text{SST}_{\text{onlineM}}$ denotes model SST computed at every time step. Time dependency is omitted for variables that follow a smooth seasonal cycle.

Equation (A1) is the formulation used to perform our multiyear climatological run. Using more elaborate bulk formulation to compute heat fluxes instead has not led to any improvement in the representation of SST and SML depth (not shown). In the synoptic simulations, using Eq. (A1) would produce an artificial feedback because the development of model SST synoptic anomalies would modify Q_{climM} , typically $\pm 30 \text{ W m}^{-2}$ for $\mp 1^\circ\text{C}$ anomaly. To circumvent this, $\text{SST}_{\text{climO}}$ in Eq. (A1) could be replaced by a prescribed SST field taking account of the synoptic forcing on SST. But this would require an a priori knowledge of the ocean SST response which we do not have. In addition, formulation of m_2 in Eq. (A1) would lead to different net air–sea heat fluxes for different ensemble members. Therefore, we choose to shift to a different formulation for Q_{clim} that does not involve any online restoring to SST, has a minimal effect on Eq. (A1)'s version of Q_{clim} , and ensures that all ensemble runs will be identically forced. To do so, we replace m_2 with $m_{2\text{adj}}$ defined as follows:

$$m_{2\text{adj}} = \frac{dQ}{d\text{SST}}(\text{SST}_{\text{climM}} - \text{SST}_{\text{climO}}), \quad (\text{A2})$$

$$Q_{\text{clim}} = m_1 + m_{2\text{adj}}. \quad (\text{A3})$$

In $m_{2\text{adj}}$, $\text{SST}_{\text{climM}}$ is the SST diagnosed from the climatological simulations. Replacing $\text{SST}_{\text{onlineM}}$ with $\text{SST}_{\text{climM}}$ ensures that m_2 and $m_{2\text{adj}}$ are identical when sufficient averaging is performed, e.g., formulation Eq. (A1) averaged over a large number of ensemble runs is equivalent to formulation Eq. (A3). Equation (A3) adjusted heat fluxes are applied on initial states obtained from climatological simulations run with Eq. (A1) (see section 2c). To preserve exact continuity of Q_{clim} at restart time (14 February), we create a transition period to smoothly shift from Eqs. (A1) to (A3). This transition is performed using two linear ramps f_{down} (from 1 to 0) and f_{up} (from 0 to 1) respectively applied to m_2 and $m_{2\text{adj}}$ between 15 February and 1 March. The same method is used for the surface freshwater flux formulation during synoptic simulations. For heat flux, the complete formulation includes the synoptic anomaly and writes:

$$Q_{\text{SF}}(t) = m_1 + f_{\text{down}}(t)m_2 + f_{\text{up}}(t)m_{2\text{adj}} + f(t)Q'_{\text{SF}}. \quad (\text{A4})$$

APPENDIX B

Melax Data Processing and Temperature Vertical Profiles

a. Melax data processing

We are not concerned with high-frequency (e.g., intradaily) variability. The temporal resolution of Melax data is degraded to 1 day. This is done with a straightforward daily averaging for ADCP currents and atmospheric variables. A more complex processing is chosen for temperature because its vertical profile is modulated by the diurnal shortwave cycle and generation of warm surface layers whereas model temperature is not. To limit model–data discrepancies arising from this difference, the most vertically mixed temperature profile at Melax is selected for every day of interest. The maximum mixing criterion is based on the temperature difference between 1 and 10 m deep: $T(z)|_{\min[T(z=1\text{m}) - T(z=10\text{m})]}$. We choose 10 m as it is a commonly used depth of reference for SMLs (de Boyer Montégut et al. 2004). This procedure typically amounts to choosing nighttime Melax in situ profiles because near-surface diurnal warming effects are then absent.

b. Melax temperature vertical profiles

The Melax dataset comprises a limited number of upwelling wind intensification and relaxation events (Fig. 4c). For each of them, the real ocean initial state and wind forcing history (before and during the event) differ from our idealized simulations (see Fig. 5). Therefore, pending more observations, model evaluation can only be done qualitatively. We have selected the upwelling intensification and the relaxation events whose wind history appeared most consistent with our synthetic forcings. The level of agreement for the wind prior to the event is better for the relaxation than for the intensification. In the latter, the observed initial state (first three days) is characterized by a relaxed wind which certainly contributes to enhancing the amplitude of the synoptic temperature response (approximately a factor of 2 larger in the observations than in the model runs with synthetic forcing anomalies). Model–data agreement is much better for the relaxation except toward the end of the event, but this is presumably again related to the fact that the meridional wind in the selected observed event and in our synthetic forcings behave quite differently (cf. Figs. 5d,h). Overall, qualitative agreement between observed and modeled vertical temperature profiles shows the ability of our simulations to reproduce real ocean processes.

REFERENCES

- Aguirre, C., R. D. Garreaud, and J. A. Rutllant, 2014: Surface ocean response to synoptic-scale variability in wind stress and heat fluxes off south-central Chile. *Dyn. Atmos. Oceans*, **65**, 64–85, <https://doi.org/10.1016/j.dynatmoce.2013.11.001>.
- , M. Rojas, R. D. Garreaud, and D. A. Rahn, 2019: Role of synoptic activity on projected changes in upwelling-favourable winds at the ocean's eastern boundaries. *npj Climate Atmos. Sci.*, **2**, 44, <https://doi.org/10.1038/s41612-019-0101-9>.

- , R. Garreaud, L. Belmar, L. Farías, L. Ramajo, and F. Barrera, 2021: High-frequency variability of the surface ocean properties off central Chile during the upwelling season. *Front. Mar. Sci.*, **8**, 702051, <https://doi.org/10.3389/fmars.2021.702051>.
- Bane, J. M., Y. H. Spitz, R. M. Letelier, and W. T. Peterson, 2007: Jet stream intraseasonal oscillations drive dominant ecosystem variations in Oregon's summertime coastal upwelling system. *Proc. Natl. Acad. Sci. USA*, **104**, 13 262–13 267, <https://doi.org/10.1073/pnas.0700926104>.
- Barnier, B., L. Siefridt, and P. Marchesiello, 1995: Thermal forcing for a global ocean circulation model using a three-year climatology of ECMWF analyses. *J. Mar. Syst.*, **6**, 363–380, [https://doi.org/10.1016/0924-7963\(94\)00034-9](https://doi.org/10.1016/0924-7963(94)00034-9).
- Barrier, N., J. Deshayes, A.-M. Treguier, and C. Cassou, 2015: Heat budget in the North Atlantic subpolar gyre: Impacts of atmospheric weather regimes on the 1995 warming event. *Prog. Oceanogr.*, **130**, 75–90, <https://doi.org/10.1016/j.pocean.2014.10.001>.
- Barth, J. A., S. D. Pierce, and R. L. Smith, 2000: A separating coastal upwelling jet at Cape Blanco, Oregon and its connection to the California Current System. *Deep-Sea Res. II*, **47**, 783–810, [https://doi.org/10.1016/S0967-0645\(99\)00127-7](https://doi.org/10.1016/S0967-0645(99)00127-7).
- , —, and R. M. Castelao, 2005: Time-dependent, wind-driven flow over a shallow midshelf submarine bank. *J. Geophys. Res.*, **110**, C10S05, <https://doi.org/10.1029/2004JC002761>.
- Beckmann, A., 1998: The representation of bottom boundary layer processes in numerical ocean circulation models. *Ocean Modeling and Parameterization*, E. P. Chassignet and J. Veron, Eds., NATO Science Series, Vol. 516, Springer, 135–154, https://doi.org/10.1007/978-94-011-5096-5_5.
- Cambon, G., 2008: Etude numérique de la mer d'Iroise: Dynamique, variabilité du front d'Ouessant et évaluation des échanges cross-frontaux. Ph.D. thesis, Université de Bretagne occidentale, 196 pp., <https://tel.archives-ouvertes.fr/tel-00976378>.
- Capet, X., E. J. Campos, and A. M. Paiva, 2008a: Submesoscale activity over the Argentinian shelf. *Geophys. Res. Lett.*, **35**, L15605, <https://doi.org/10.1029/2008GL034736>.
- , J. C. McWilliams, M. J. Molemaker, and A. F. Shchepetkin, 2008b: Mesoscale to submesoscale transition in the California Current system. Part I: Flow structure, eddy flux, and observational tests. *J. Phys. Oceanogr.*, **38**, 29–43, <https://doi.org/10.1175/2007JPO3671.1>.
- , and Coauthors, 2017: On the dynamics of the southern Senegal upwelling center: Observed variability from synoptic to superinertial scales. *J. Phys. Oceanogr.*, **47**, 155–180, <https://doi.org/10.1175/JPO-D-15-0247.1>.
- Carton, J. A., and B. S. Giese, 2008: A reanalysis of ocean climate using Simple Ocean Data Assimilation (SODA). *Mon. Wea. Rev.*, **136**, 2999–3017, <https://doi.org/10.1175/2007MWR1978.1>.
- Chabert, P., F. d'Ovidio, V. Echevin, M. R. Stukel, and M. D. Ohman, 2021: Cross-shore flow and implications for carbon export in the California Current ecosystem: A Lagrangian analysis. *J. Geophys. Res. Oceans*, **126**, e2020JC016611, <https://doi.org/10.1029/2020JC016611>.
- Chavez, F. P., and M. Messié, 2009: A comparison of eastern boundary upwelling ecosystems. *Prog. Oceanogr.*, **83**, 80–96, <https://doi.org/10.1016/j.pocean.2009.07.032>.
- Colas, F., X. Capet, J. C. McWilliams, and Z. Li, 2013: Mesoscale eddy buoyancy flux and eddy-induced circulation in eastern boundary currents. *J. Phys. Oceanogr.*, **43**, 1073–1095, <https://doi.org/10.1175/JPO-D-11-0241.1>.
- Curcic, M., S. S. Chen, and T. M. Özgökmen, 2016: Hurricane-induced ocean waves and Stokes drift and their impacts on surface transport and dispersion in the Gulf of Mexico. *Geophys. Res. Lett.*, **43**, 2773–2781, <https://doi.org/10.1002/2015GL067619>.
- de Boyer Montégut, C., G. Madec, A. S. Fischer, A. Lazar, and D. Iudicone, 2004: Mixed layer depth over the global ocean: An examination of profile data and a profile-based climatology. *J. Geophys. Res.*, **109**, C12003, <https://doi.org/10.1029/2004JC002378>.
- Debreu, L., and E. Blayo, 2008: Two-way embedding algorithms: A review. *Ocean Dyn.*, **58**, 415–428, <https://doi.org/10.1007/s10236-008-0150-9>.
- , P. Marchesiello, P. Penven, and G. Cambon, 2012: Two-way nesting in split-explicit ocean models: Algorithms, implementation and validation. *Ocean Modell.*, **49–50**, 1–21, <https://doi.org/10.1016/j.ocemod.2012.03.003>.
- Desbiolles, F., B. Blanke, and A. Bentamy, 2014: Short-term upwelling events at the western African coast related to synoptic atmospheric structures as derived from satellite observations. *J. Geophys. Res. Oceans*, **119**, 461–483, <https://doi.org/10.1002/2013JC009278>.
- Deshayes, J., R. Curry, and R. Msadek, 2014: CMIP5 model inter-comparison of freshwater budget and circulation in the North Atlantic. *J. Climate*, **27**, 3298–3317, <https://doi.org/10.1175/JCLI-D-12-00700.1>.
- Dong, J., B. Fox-Kemper, H. Zhang, and C. Dong, 2020: The scale of submesoscale baroclinic instability globally. *J. Phys. Oceanogr.*, **50**, 2649–2667, <https://doi.org/10.1175/JPO-D-20-0043.1>.
- Dorman, J. G., S. Bollens, and A. Slaughter, 2005: Population biology of euphausiids off Northern California and effects of short time-scale wind events on Euphausia Pacifica. *Mar. Ecol. Prog. Ser.*, **288**, 183–198, <https://doi.org/10.3354/meps288183>.
- Echevin, V., F. Colas, D. Espinoza-Morriberon, L. Vasquez, T. Anculle, and D. Gutierrez, 2018: Forcings and evolution of the 2017 coastal El Niño off northern Peru and Ecuador. *Front. Mar. Sci.*, **5**, 367, <https://doi.org/10.3389/fmars.2018.00367>.
- , J. Hauschildt, F. Colas, S. Thomsen, and O. Aumont, 2021: Impact of chlorophyll shading on the Peruvian upwelling system. *Geophys. Res. Lett.*, **48**, e2021GL094429, <https://doi.org/10.1029/2021GL094429>.
- Evans, W., B. Hales, P. G. Strutton, R. K. Shearman, and J. A. Barth, 2015: Failure to bloom: Intense upwelling results in negligible phytoplankton response and prolonged CO₂ outgassing over the Oregon shelf. *J. Geophys. Res. Oceans*, **120**, 1446–1461, <https://doi.org/10.1002/2014JC010580>.
- Farneti, R., T. L. Delworth, A. J. Rosati, S. M. Griffies, and F. Zeng, 2010: The role of mesoscale eddies in the rectification of the Southern Ocean response to climate change. *J. Phys. Oceanogr.*, **40**, 1539–1557, <https://doi.org/10.1175/2010JPO4353.1>.
- Fearon, G., S. Herbette, J. Veitch, G. Cambon, A. J. Lucas, F. Lemarié, and M. Vichi, 2020: Enhanced vertical mixing in coastal upwelling systems driven by diurnal-inertial resonance: Numerical experiments. *J. Geophys. Res. Oceans*, **125**, e2020JC016208, <https://doi.org/10.1029/2020JC016208>.
- Ferreira Cordeiro, N. G., J. Dubert, R. Nolasco, and E. D. Barton, 2018: Transient response of the northwestern Iberian upwelling regime. *PLOS ONE*, **13**, e0197627, <https://doi.org/10.1371/journal.pone.0197627>.
- Fox-Kemper, B., R. Ferrari, and R. Hallberg, 2008: Parameterization of mixed layer eddies. Part I: Theory and diagnosis. *J. Phys. Oceanogr.*, **38**, 1145–1165, <https://doi.org/10.1175/2007JPO3792.1>.
- Gan, J., and J. S. Allen, 2002a: A modeling study of shelf circulation off Northern California in the region of the coastal ocean dynamics experiment 2. Simulations and comparisons

- with observations. *J. Geophys. Res.*, **107**, 3184, <https://doi.org/10.1029/2001JC001190>.
- , and —, 2002b: A modeling study of shelf circulation off Northern California in the region of the coastal ocean dynamics experiment: Response to relaxation of upwelling winds. *J. Geophys. Res.*, **107**, 3123, <https://doi.org/10.1029/2000JC000768>.
- , and —, 2005a: Modeling upwelling circulation off the Oregon coast. *J. Geophys. Res.*, **110**, C10S07, <https://doi.org/10.1029/2004JC002692>.
- , and —, 2005b: On open boundary conditions for a limited-area coastal model off Oregon. Part 1: Response to idealized wind forcing. *Ocean Modell.*, **8**, 115–133, <https://doi.org/10.1016/j.ocemod.2003.12.006>.
- García-Reyes, M., J. L. Largier, and W. J. Sydeman, 2014: Synoptic-scale upwelling indices and predictions of phyto- and zooplankton populations. *Prog. Oceanogr.*, **120**, 177–188, <https://doi.org/10.1016/j.pcean.2013.08.004>.
- Garstang, M., 1967: Sensible and latent heat exchange in low latitude synoptic scale systems. *Tellus*, **19A**, 492–508, <https://doi.org/10.1111/j.2153-3490.1967.tb01504.x>.
- Hersbach, H., and Coauthors, 2018: ERA5 hourly data on single levels from 1979 to present. Copernicus Climate Change Service (C3S) Climate Data Store (CDS), accessed 9 December 2020, <https://doi.org/10.24381/cds.adbb2d47>.
- Hetland, R. D., 2017: Suppression of baroclinic instabilities in buoyancy-driven flow over sloping bathymetry. *J. Phys. Oceanogr.*, **47**, 49–68, <https://doi.org/10.1175/JPO-D-15-0240.1>.
- Hilt, M., and Coauthors, 2020: Numerical modelling of hydraulic control, solitary waves and primary instabilities in the Strait of Gibraltar. *Ocean Modell.*, **151**, 101642, <https://doi.org/10.1016/j.ocemod.2020.101642>.
- Jullien, S., and Coauthors, 2012: Impact of tropical cyclones on the heat budget of the South Pacific Ocean. *J. Phys. Oceanogr.*, **42**, 1882–1906, <https://doi.org/10.1175/JPO-D-11-0133.1>.
- Kobashi, D., and R. Hetland, 2020: Reproducibility and variability of submesoscale frontal eddies on a broad, low-energy shelf of freshwater influence. *Ocean Dyn.*, **70**, 1377–1395, <https://doi.org/10.1007/s10236-020-01401-4>.
- Kounta Diop, L., 2019: Le rôle de la dynamique océanique et atmosphérique en Atlantique Nord sur le fonctionnement de l'upwelling ouest-africain. Ph.D. thesis, Sorbonne Université, 175 pp., <https://www.theses.fr/2019SORUS649>.
- Kuebel Cervantes, B. T., and J. S. Allen, 2006: Numerical model simulations of continental shelf flows off Northern California. *Deep-Sea Res. II*, **53**, 2956–2984, <https://doi.org/10.1016/j.dsr2.2006.07.004>.
- Lapeyre, G., and P. Klein, 2006: Impact of the small-scale elongated filaments on the oceanic vertical pump. *J. Mar. Res.*, **64**, 835–851, <https://doi.org/10.1357/002224006779698369>.
- Large, W. G., J. C. McWilliams, and S. C. Doney, 1994: Oceanic vertical mixing: A review and a model with a nonlocal boundary layer parameterization. *Rev. Geophys.*, **32**, 363–403, <https://doi.org/10.1029/94RG01872>.
- Largier, J. L., 2020: Upwelling bays: How coastal upwelling controls circulation, habitat, and productivity in bays. *Annu. Rev. Mar. Sci.*, **12**, 415–447, <https://doi.org/10.1146/annurev-marine-010419-011020>.
- , and Coauthors, 2006: WEST: A Northern California study of the role of wind-driven transport in the productivity of coastal plankton communities. *Deep-Sea Res. II*, **53**, 2833–2849, <https://doi.org/10.1016/j.dsr2.2006.08.018>.
- Lentz, S. J., 1987: A heat budget for the Northern California shelf during CODE 2. *J. Geophys. Res.*, **92**, 14 491–14 509, <https://doi.org/10.1029/JC092iC13p14491>.
- Lévy, M., P. Klein, and A.-M. Treguier, 2001: Impact of submesoscale physics on production and subduction of phytoplankton in an oligotrophic regime. *J. Mar. Res.*, **59**, 535–565, <https://doi.org/10.1357/002224001762842181>.
- Lopes, J. F., J. A. Ferreira, A. C. Cardoso, and A. C. Rocha, 2014: Variability of temperature and chlorophyll of the Iberian Peninsula near coastal ecosystem during an upwelling event for the present climate and a future climate scenario. *J. Mar. Syst.*, **129**, 271–288, <https://doi.org/10.1016/j.jmarsys.2013.07.002>.
- Machu, E., and Coauthors, 2019: First evidence of anoxia and nitrogen loss in the southern canary upwelling system. *Geophys. Res. Lett.*, **46**, 2619–2627, <https://doi.org/10.1029/2018GL079622>.
- Marchesiello, P., J. C. McWilliams, and A. Shchepetkin, 2003: Equilibrium structure and dynamics of the California Current system. *J. Phys. Oceanogr.*, **33**, 753–783, [https://doi.org/10.1175/1520-0485\(2003\)33<753:ESADOT>2.0.CO;2](https://doi.org/10.1175/1520-0485(2003)33<753:ESADOT>2.0.CO;2).
- McCabe, R. M., B. M. Hickey, E. P. Dever, and P. MacCready, 2015: Seasonal cross-shelf flow structure, upwelling relaxation, and the alongshelf pressure gradient in the Northern California Current system. *J. Phys. Oceanogr.*, **45**, 209–227, <https://doi.org/10.1175/JPO-D-14-0025.1>.
- McWilliams, J. C., 2016: Submesoscale currents in the ocean. *Proc. Roy. Soc.*, **472**, 20160117, <https://doi.org/10.1098/rspa.2016.0117>.
- Montgomery, R. B., 1974: Comments on ‘Seasonal variability of the Florida Current’, by Niiler and Richardson. *J. Mar. Sci.*, **32**, 533–534.
- Morgan, S. G., S. H. Miller, M. J. Robart, and J. L. Largier, 2018: Nearshore larval retention and cross-shelf migration of benthic crustaceans at an upwelling center. *Front. Mar. Sci.*, **5**, 161, <https://doi.org/10.3389/fmars.2018.00161>.
- Narimousa, S., and T. Maxworthy, 1989: Application of a laboratory model to the interpretation of satellite and field observations of coastal upwelling. *Dyn. Atmos. Oceans*, **13**, 1–46, [https://doi.org/10.1016/0377-0265\(89\)90032-8](https://doi.org/10.1016/0377-0265(89)90032-8).
- NASA, 2014: NASA Goddard Space Flight Center, Ocean Ecology Laboratory, Ocean Biology Processing Group. Moderate-resolution Imaging Spectroradiometer (MODIS) Aqua 11 μ m Day/Night Sea Surface Temperature Data. NASA OB.DAAC, accessed 25 November 2020, <https://oceancolor.gsfc.nasa.gov/data/10.5067/AQUA/MODIS/L3M/SST/2014/>.
- Ndoye, S., X. Capet, P. Estrade, B. Sow, D. Dagorne, A. Lazar, A. Gaye, and P. Brehmer, 2014: SST patterns and dynamics of the Southern Senegal-Gambia Upwelling Center. *J. Geophys. Res. Oceans*, **119**, 8315–8335, <https://doi.org/10.1002/2014JC010242>.
- , —, —, —, E. Machu, T. Brochier, J. Döring, and P. Brehmer, 2017: Dynamics of a “low-enrichment high-retention” upwelling center over the Southern Senegal shelf. *Geophys. Res. Lett.*, **44**, 5034–5043, <https://doi.org/10.1002/2017GL072789>.
- Okumura, Y. M., T. Sun, and X. Wu, 2017: Asymmetric modulation of El Niño and La Niña and the linkage to tropical Pacific decadal variability. *J. Climate*, **30**, 4705–4733, <https://doi.org/10.1175/JCLI-D-16-0680.1>.
- Penven, P., V. Echevin, J. Pasapera, F. Colas, and J. Tam, 2005: Average circulation, seasonal cycle, and mesoscale dynamics of the Peru Current system: A modeling approach. *J. Geophys. Res.*, **110**, C10021, <https://doi.org/10.1029/2005JC002945>.

- Philander, S. G. H., and J.-H. Yoon, 1982: Eastern boundary currents and coastal upwelling. *J. Phys. Oceanogr.*, **12**, 862–879, [https://doi.org/10.1175/1520-0485\(1982\)012<0862:EBCACU>2.0.CO;2](https://doi.org/10.1175/1520-0485(1982)012<0862:EBCACU>2.0.CO;2).
- Pitcher, G. C., D. R. Walker, B. A. Mitchell-Innes, and C. L. Moloney, 1991: Short-term variability during an anchor station study in the southern Benguela upwelling system: Phytoplankton dynamics. *Prog. Oceanogr.*, **28**, 39–64, [https://doi.org/10.1016/0079-6611\(91\)90020-M](https://doi.org/10.1016/0079-6611(91)90020-M).
- Polo, I., A. Lazar, B. Rodriguez-Fonseca, and S. Arnault, 2008: Oceanic Kelvin waves and tropical Atlantic intraseasonal variability: 1. Kelvin wave characterization. *J. Geophys. Res.*, **113**, C07009, <https://doi.org/10.1029/2007JC004495>.
- Pringle, J. M., 2002: Enhancement of wind-driven upwelling and downwelling by alongshore bathymetric variability. *J. Phys. Oceanogr.*, **32**, 3101–3112, [https://doi.org/10.1175/1520-0485\(2002\)032<3101:EOWDUA>2.0.CO;2](https://doi.org/10.1175/1520-0485(2002)032<3101:EOWDUA>2.0.CO;2).
- Ramos, A. M., A. C. Pires, P. M. Sousa, and R. M. Trigo, 2013: The use of circulation weather types to predict upwelling activity along the western Iberian Peninsula coast. *Cont. Shelf Res.*, **69**, 38–51, <https://doi.org/10.1016/j.csr.2013.08.019>.
- Ramp, S. R., J. D. Paduan, I. Shulman, J. Kindle, F. L. Bahr, and F. Chavez, 2005: Observations of upwelling and relaxation events in the northern Monterey Bay during August 2000. *J. Geophys. Res.*, **110**, C07013, <https://doi.org/10.1029/2004JC002538>.
- Relvas, P., and E. D. Barton, 2005: A separated jet and coastal counterflow during upwelling relaxation off Cape São Vicente (Iberian Peninsula). *Cont. Shelf Res.*, **25**, 29–49, <https://doi.org/10.1016/j.csr.2004.09.006>.
- Renault, L., J. C. McWilliams, F. Kessouri, A. Jousse, H. Frenzel, R. Chen, and C. Deutsch, 2021: Evaluation of high-resolution atmospheric and oceanic simulations of the California Current system. *Prog. Oceanogr.*, **195**, 102564, <https://doi.org/10.1016/j.pcean.2021.102564>.
- Risien, C. M., and D. B. Chelton, 2008: A global climatology of surface wind and wind stress fields from eight years of QuikSCAT scatterometer data. *J. Phys. Oceanogr.*, **38**, 2379–2413, <https://doi.org/10.1175/2008JPO3881.1>.
- Rodi, W., 1987: Examples of calculation methods for flow and mixing in stratified fluids. *J. Geophys. Res.*, **92**, 5305–5328, <https://doi.org/10.1029/JC092iC05p05305>.
- Roy, C., 1989: Fluctuations des vents et variabilité de l'upwelling devant les côtes du Sénégal. *Oceanol. Acta*, **12**, 361–369.
- , 1998: An upwelling-induced retention area off Senegal: A mechanism to link upwelling and retention processes. *S. Afr. J. Mar. Sci.*, **19**, 89–98, <https://doi.org/10.2989/025776198784126881>.
- Send, U., 1989: The origin of eddy heat fluxes in the Northern California upwelling regime. *J. Geophys. Res.*, **94**, 871–876, <https://doi.org/10.1029/JC094iC01p00871>.
- , and S. Nam, 2012: Relaxation from upwelling: The effect on dissolved oxygen on the continental shelf. *J. Geophys. Res.*, **117**, C04024, <https://doi.org/10.1029/2011JC007517>.
- , R. C. Beardsley, and C. D. Winant, 1987: Relaxation from upwelling in the coastal ocean dynamics experiment. *J. Geophys. Res.*, **92**, 1683–1698, <https://doi.org/10.1029/JC092iC02p01683>.
- Shanks, A. L., S. G. Morgan, J. MacMahan, A. J. H. M. Reniers, M. Jarvis, J. Brown, A. Fujimura, and C. Griesemer, 2014: Onshore transport of plankton by internal tides and upwelling-relaxation events. *Mar. Ecol. Prog. Ser.*, **502**, 39–51, <https://doi.org/10.3354/meps10717>.
- Shchepetkin, A. F., and J. C. McWilliams, 2005: The Regional Oceanic Modeling System (ROMS): A split-explicit, free-surface, topography-following-coordinate oceanic model. *Ocean Modell.*, **9**, 347–404, <https://doi.org/10.1016/j.ocemod.2004.08.002>.
- , and —, 2009: Correction and commentary for “Ocean forecasting in terrain-following coordinates: Formulation and skill assessment of the regional ocean modeling system” by Haidvogel et al., *J. Comp. Phys.* **227**, pp. 3595–3624. *J. Comput. Phys.*, **228**, 8985–9000, <https://doi.org/10.1016/j.jcp.2009.09.002>.
- Stukel, M. R., and Coauthors, 2017: Mesoscale ocean fronts enhance carbon export due to gravitational sinking and subduction. *Proc. Natl. Acad. Sci. USA*, **114**, 1252–1257, <https://doi.org/10.1073/pnas.1609435114>.
- Sultan, B., and S. Janicot, 2003: The West African monsoon dynamics. Part II: The “Preonset” and “Onset” of the summer monsoon. *J. Climate*, **16**, 3407–3427, [https://doi.org/10.1175/1520-0442\(2003\)016<3407:TWAMDP>2.0.CO;2](https://doi.org/10.1175/1520-0442(2003)016<3407:TWAMDP>2.0.CO;2).
- Tall, A. W., E. Machu, V. Echevin, X. Capet, A. Pietri, K. Corr  a, S. M. Sall, and A. Lazar, 2021: Variability of dissolved oxygen in the bottom layer of the Southern Senegalese shelf. *J. Geophys. Res. Oceans*, **126**, e2020JC016854, <https://doi.org/10.1029/2020JC016854>.
- Thomsen, S., X. Capet, and V. Echevin, 2021: Competition between baroclinic instability and Ekman transport under varying buoyancy forcings in upwelling systems: An idealized analog to the Southern Ocean. *J. Phys. Oceanogr.*, **51**, 3347–3364, <https://doi.org/10.1175/JPO-D-20-0294.1>.
- Torres, R., D. R. Turner, N. Silva, and J. Rutllant, 1999: High short-term variability of CO₂ fluxes during an upwelling event off the Chilean coast at 30°S. *Deep-Sea Res. I*, **46**, 1161–1179, [https://doi.org/10.1016/S0967-0637\(99\)00003-5](https://doi.org/10.1016/S0967-0637(99)00003-5).
- , D. Turner, J. Rutllant, M. Sobarzo, T. Antezana, and H. E. Gonzalez, 2002: CO₂ outgassing off central Chile (31–30°S) and Northern Chile (24–23°S) during austral summer 1997: The effect of wind intensity on the upwelling and ventilation of CO₂-rich waters. *Deep-Sea Res. I*, **49**, 1413–1429, [https://doi.org/10.1016/S0967-0637\(02\)00034-1](https://doi.org/10.1016/S0967-0637(02)00034-1).
- Umlauf, L., and H. Burchard, 2003: A generic length-scale equation for geophysical turbulence models. *J. Mar. Res.*, **61**, 235–265, <https://doi.org/10.1357/00222400322005087>.
- Van Roekel, L., and Coauthors, 2018: The KPP boundary layer scheme for the ocean: Revisiting its formulation and benchmarking one-dimensional simulations relative to LES. *J. Adv. Model. Earth Syst.*, **10**, 2647–2685, <https://doi.org/10.1029/2018MS001336>.
- Wang, D.-P., 1993: Model of frontogenesis: Subduction and upwelling. *J. Mar. Res.*, **51**, 497–513, <https://doi.org/10.1357/002224093224034>.
- Wijesekera, H. W., J. S. Allen, and P. A. Newberger, 2003: Modeling study of turbulent mixing over the continental shelf: Comparison of turbulent closure schemes. *J. Geophys. Res.*, **108**, 3103, <https://doi.org/10.1029/2001JC001234>.
- Wing, S. R., L. W. Botsford, J. L. Largier, and L. E. Morgan, 1995: Spatial structure of relaxation events and crab settlement in the Northern California upwelling system. *Mar. Ecol. Prog. Ser.*, **128**, 199–211, <https://doi.org/10.3354/meps128199>.
- Worley, S. J., S. D. Woodruff, R. W. Reynolds, S. J. Lubker, and N. Lott, 2005: ICOADS release 2.1 data and products. *Int. J. Climatol.*, **25**, 823–842, <https://doi.org/10.1002/joc.1166>.
- Zhang, Y., J. G. Bellingham, J. P. Ryan, and M. A. Godin, 2015: Evolution of a physical and biological front from upwelling to relaxation. *Cont. Shelf Res.*, **108**, 55–64, <https://doi.org/10.1016/j.csr.2015.08.005>.
- Zimmerman, J. T. F., 1986: The tidal whirlpool: A review of horizontal dispersion by tidal and residual currents. *Neth. J. Sea Res.*, **20**, 133–154, [https://doi.org/10.1016/0077-7579\(86\)90037-2](https://doi.org/10.1016/0077-7579(86)90037-2).